Technical University of Munich

Department of Physics

Bachelor's Thesis in Physics

Schlieren and Shadowgraphy Imaging Studies for the Characterization of a Plasma Column

By

Felix Wechsler

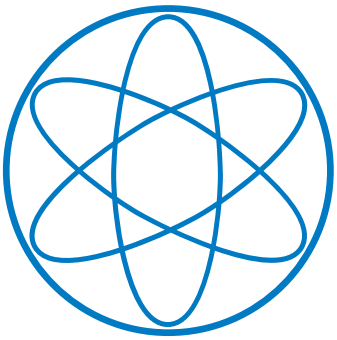

Technical University of Munich

Department of Physics

Bachelor's Thesis in Physics

Schlieren und Shadowgraphy Imaging Studies for the Characterization of a Plasma Column

Schlieren- und Schattenverfahren-Bildgebungsstudien zur Charakterisierung von Plasmasäulen

Author: Felix Wechsler

Supervisor: Prof. Dr. rer. nat. Allen Caldwell

Advisors: PhD. Joshua Moody

M. Sc. Anna-Maria Bachmann

Submission date: September 11, 2019

Contents

1. Abstract

The advanced wakefield experiment (AWAKE) is a proof of principle experiment located at CERN. It is the first plasma wakefield accelerator which uses a proton bunch as driver. The main purpose is the acceleration of electrons to several GeV over a distance of 10 m. A schlieren setup is used for the determination of the diameter of a plasma column located in rubidium vapor, we apply schlieren and shadowgraphy techniques on well known optical targets like cylindrical lenses or glass capillaries. The measurements of the well known targets are compared to numerical simulations of both setups. Furthermore, we perform simulations of a sharp edged and a fuzzy plasma column. The obtained results can be applied to the rubidium plasma measurements at CERN.

2. Introduction to AWAKE

The idea of plasma wakefield accelerators was born in 1979 [TD79]. Plasma accelerators are especially favored for acceleration of electrons. Since the synchrotron radiation continuously emits photons and is inverse proportional to m_e^4 circular accelerators are not used to accelerate electrons to the TeV scale. Conventional linear colliders are very long and expensive for acceleration up to several TeV. Therefore, the concept of linear wakefield accelerators was of great interest in the last decades. Recent results reached up to 4.25 GeV over 2 cm [Blu+07]. In 2009 Caldwell [Cal+09] discussed the possibility of using a proton bunch as driver to accelerate electrons.

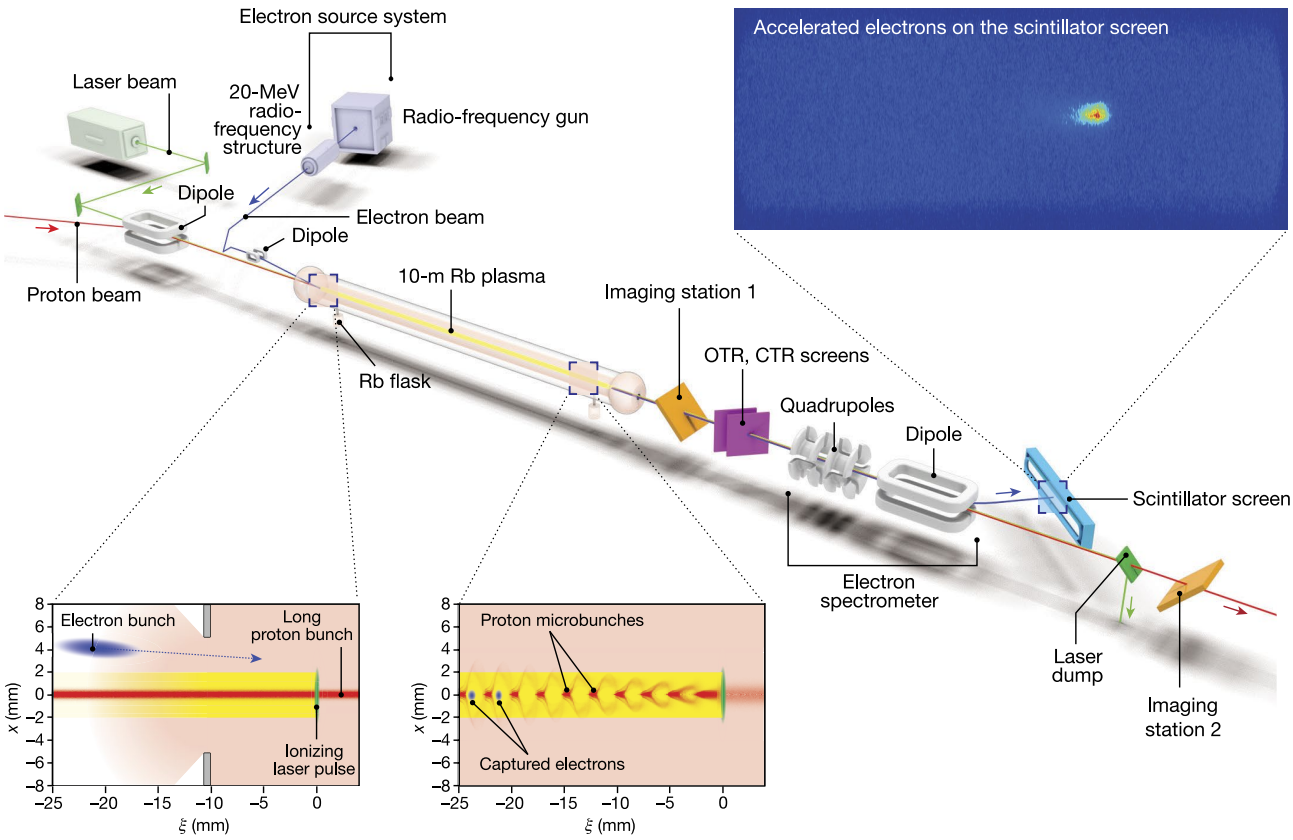

Figure 2.1.: The AWAKE setup [Adl+18].

In 2018, AWAKE achieved an acceleration of electrons up to 2 GeV over a distance of 10 m

[Adl+18]. In this section we give a short overview over the AWAKE experiment in general. After that we discuss the laser ionized plasma column and the parameters that are relevant to image it using schlieren and shadowgraphy techniques.

2.1. Concept and Experimental Setup

The general setup of AWAKE at CERN can be seen in Figure 2.1. On the left hand side we can see the Super Proton Synchrotron (SPS) proton bunch of 400 GeV with a RMS bunch length of (6-12) cm and a radial diameter of 200 µm. The 10 m long tube is filled with rubidium vapor. Protons are injected into the plasma along with the laser pulse which is in the middle of the proton bunch. The laser ionizes the rubidium vapor and creates the plasma. Due to a process called seeded self-modulation [KPL10] the proton bunch separates in several focused and defocused regions. The focused regions can be understood like several microbunches. Electrons are then placed between two microbunches into the accelerating region. The radius of the plasma column must exceed the radial size of the proton bunch. Hence, we attempt to develop a technique to determine the plasma column radius.

2.2. Plasma Column

[Bac+18a] and [Bac+18b] contain results on the determination of the plasma column. The latter gives us the current optical setup for the determination of the plasma column. Figure 2.2 shows

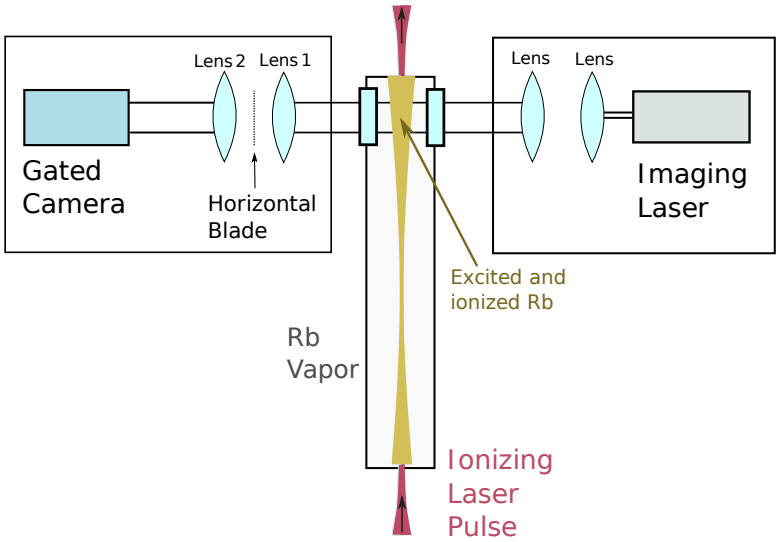

Figure 2.2.: Current Schlieren setup at AWAKE experiment. Figure take from [Bac+18b].

this experimental setup in detail. The diagnostics of the plasma is performed at the end of the

vapor source. For the Schlieren measurements an imaging laser (CW laser DLC DL pro from TOPTICA[1]) is used. The wavelength is tunable up to a precision of 10 kHz around the 780 nm transition wavelength of rubidium. The property of tuning the probe laser is useful because the refractive index of non-excited rubidium vapor depends on the wavelength of the laser. A schematic cross section of the plasma column can be seen in Figure 2.3. The outermost layer is non-excited rubidium vapor and the next layer is a ring of excited but not ionized rubidium vapor. The inner circle is a singly ionized plasma column. From now on we assume a thin layer of excited rubidium vapor and neglect it in our considerations.

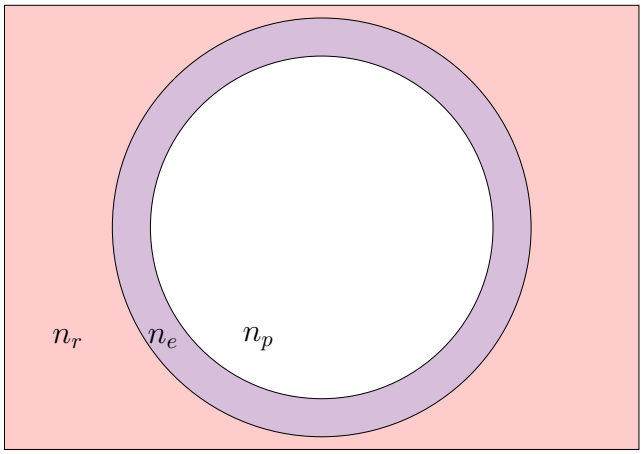

Figure 2.3.: Cross section with non-excited rubidium (red), excited rubidium (purple) and singly ionized rubidium plasma (white).

Equation 2.1 is given by [Dem07] and allows to calculate the refractive index of the non-excited rubidium layer:

$$n_r = \sqrt{1 + \frac{N_k e^2}{\varepsilon_0 m_e} \sum_{k \neq l} \frac{f_{kl}}{\omega_{kl}^2 - \omega^2 + i\gamma_{kl}\omega}} \tag{2.1}$$

where N_k being the number of electrons in lower state l, f_{kl} the oscillator strength of the transition, ω_{kl} the transition frequency from state k to l and $\gamma_{kl} = \frac{1}{\tau_{kl}}$ with τ_{kl} the lifetime of the upper state k. The refractive index dependency on the probe laser detuning frequency can be seen in Figure 2.4. Note that we neglect the hyperfine structure close to the transition wavelength. The parameter values are taken from [Ste]. The refractive index for plasma is given by [Pie10]:

$$n_p = \sqrt{1 - \frac{\omega_p^2}{\omega^2}} \tag{2.2}$$

ω is the probe laser frequency and ω_p is the plasma frequency. The plasma frequency is in the order of $\omega_p \approx 2000\,\mathrm{GHz}$ [CER+19] and the probe laser frequency is given by $\omega = \frac{2\pi c}{780\,\mathrm{nm}} \approx 2.4\,\mathrm{PHz}$.

[1] https://www.toptica.com/products/tunable-diode-lasers/ecdl-dfb-lasers/dl-pro/

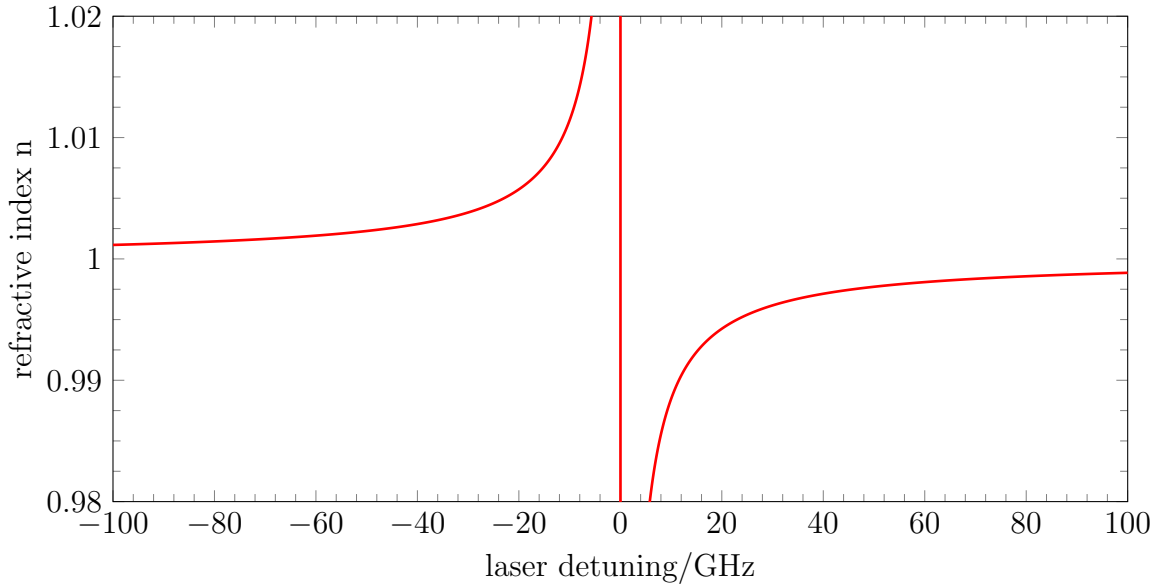

Figure 2.4.: Refractive index of rubidium vapor around the transition wavelength $\lambda = 780\,\mathrm{nm}$ neglecting hyperfine structure.

Therefore, we obtain a refractive index of the plasma of $n_p \approx 1 - 3 \cdot 10^{-7}$. Figure 2.4 shows that the refractive index of rubidium vapor is much larger for frequencies close to the transition line than the refractive index of plasma and from now on we assume $n_p = 1$. The optical properties and the possibility to determine both the diameter of the plasma column and the refractive index of the rubidium vapor column are subject of this thesis and will be discussed further in the following chapters. The experiments are conducted on well known optical targets like cylindrical lenses and glass capillaries.

3. Optical Model

In this chapter we will explain the optical model applied onto our schlieren and shadowgraphy imaging system.

3.1. Optical Properties of Plasma Column

In this section we derive the optical properties of the plasma column in the rubidium vapor, as the focal length of the plasma column. Since we assume circular symmetry and a homogeneous refractive index the column is a lens under paraxial approximation. In Figure 3.1 we assume that $n_p \approx 1$ and $n_r < n_p$ which can be achieved by using a larger wavelength than the transition line (see Figure 2.4). n_p is the refractive index of the plasma and n_r the one of rubidium vapor. Therefore, the column acts as a focusing lens. The rays are propagating from the left and focused onto a point on the right hand side of the column.

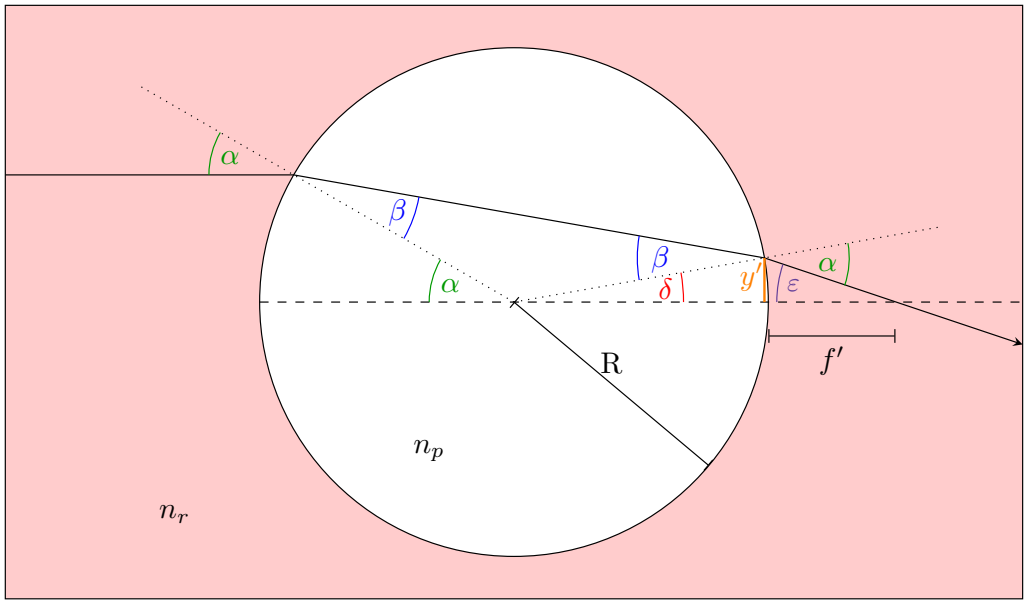

Figure 3.1.: Schematic sketch of the plasma column illuminated by a single ray from the left.

To derive the focal length we assume small angles. From Snell's law follows:

$$\alpha n_r = n_p \beta \tag{3.1}$$

Furthermore, the angle δ is:

$$\delta = 180° - \alpha - (180° - 2\beta) = 2\beta - \alpha \tag{3.2}$$

The height y' is given by:

$$y' = \delta R \tag{3.3}$$

where R is the radius of the column. The last angle we need is ε which is given by the sum of angles in a triangle:

$$\varepsilon = 180° - \delta - (180° - \alpha) = 2\alpha - 2\beta \tag{3.4}$$

Combining all we get the following for f':

$$f' = \frac{y'}{\varepsilon} = \frac{(2\beta - \alpha)R}{2\alpha - 2\beta} \tag{3.5}$$

Now the focal length with respect to the middle is:

$$f = R + f' = R + \frac{(2\beta - \alpha)R}{2\alpha - 2\beta} = \frac{Rn_p}{2(n_p - n_r)} = \frac{R}{2(1 - n_r)} \tag{3.6}$$

where the last step is valid for $n_p = 1$. We obtain that the focal length of the plasma column depends only on the refractive index of the rubidium vapor and the diameter of the plasma column. We want to determine both parameters in the following. Note that the derivations are also valid for $n_r > n_p$ being on the other side of the transition line with our probe laser detuning frequency (see Figure 2.4). However, in this case the focal length is negative and our columns acts as a diverging lens. We should mention that a column is not a perfect lens and that we will observe a lot of spherical aberrations in practice. Theoretically there is also reflection of light due to the transition between two materials. With a small difference of the refractive indices we will not observe significant loss in intensity caused by this effect. In Figure 3.2 we can see that the intensity loss gets only relevant for very steep incoming angles.

3.2. Target Selection

Since we want to remodel the plasma under known conditions we are trying to find a target which has the same optical properties.

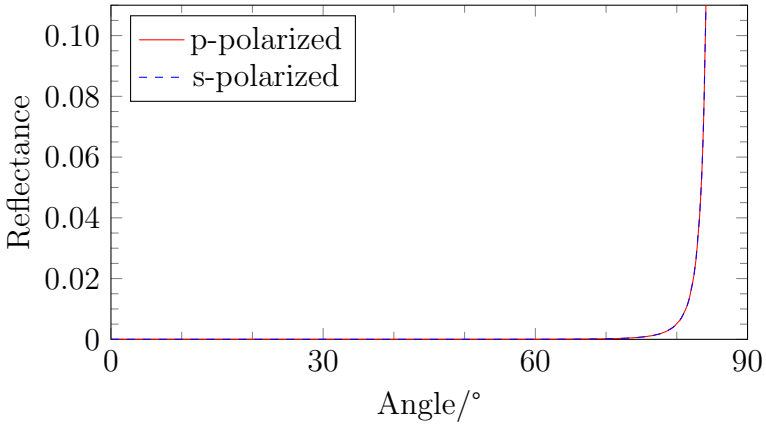

Figure 3.2.: Reflectance calculated with Fresnel equations for $n_r = 1.004$ and $n_p = 1$.

Because the diameter of the plasma is estimated to be (0.5-2) mm [Bac+18b] we want to investigate comparable small targets. Out of Equation 3.6 we can derive the focal length of a solid glass column:

$$f = \frac{R \cdot n}{2(n-1)} \tag{3.7}$$

If we insert $n = 1.5$ for glass and a radius of 1 mm, we obtain a focal length of $f = 1.5\,\text{mm}$. The diameter would be similar to that one of the plasma column but the focal length is much smaller since the focal length of the column is (with same radius and $n_r = 1 - 0.006$) $f_p = 83\,\text{mm}$. To circumvent this problem a thin glass capillary with $r_o - r_i \ll r_o$ like in Figure 3.3 can be used.

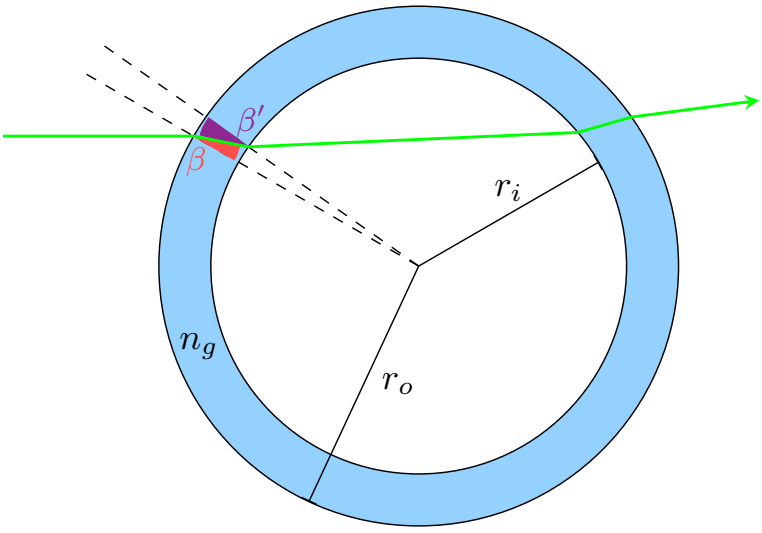

Figure 3.3.: Cross section of a glass capillary.

One can see that the glass capillary acts like a defocusing lens. Since we assume $n_g > 1$ and we place the glass capillary in air, the angle β' will be greater than β. And due to simple geometry

and Snell's law the green ray will be defocused. In this case we avoid calculating the focal length using geometry. Conceptually we can cut our glass capillary into two halves. These two halves now consist of two glass lenses with a distance roughly $d = 2r_i$. The Lensmaker's equation tells us the focal length of the first and second half.

$$\frac{1}{f} = (n-1)\left(\frac{1}{R_1} - \frac{1}{R_2}\right) \tag{3.8}$$

Furthermore, we can combine a relatively thin optical system consisting of two lenses via:

$$\frac{1}{f_{\text{res}}} = \frac{1}{f_1} + \frac{1}{f_2} - \frac{d}{f_1 f_2} \tag{3.9}$$

The focal length f_1 is calculated with:

$$\frac{1}{f} = (n-1)\left(\frac{1}{r_o} - \frac{1}{r_i}\right) \tag{3.10}$$

The focal length f_2 of the right half is identical to f_1 since we can always turn a lens around without changing the focal length. Therefore, the focal length f_{res} is:

$$f_{\text{res}} = \frac{f_1^2}{2f_1 - 2r_i} \tag{3.11}$$

Later we will see that the focal length is much longer than that of a solid glass tube and is suitable as a target for our experiments.

3.3. Schlieren Imaging

Now we introduce the schlieren imaging technique for determining differences in refractive indices of a medium. Schlieren techniques are frequently used in the context of visualising turbulences in transparent media, in most cases air. We use it for size determination.
Our medium is rubidium vapor which is also transparent. In contradiction to most applications of schlieren we assume that we have a circular symmetric column which makes it easier to get quantitative information out of the recorded images. If one is interested in a more general introduction to schlieren, we suggest [Set01].

The setup we use can be seen in Figure 3.4. Our light source is a laser. This is unusual in common schlieren setups but in our case it is necessary because the refractive index

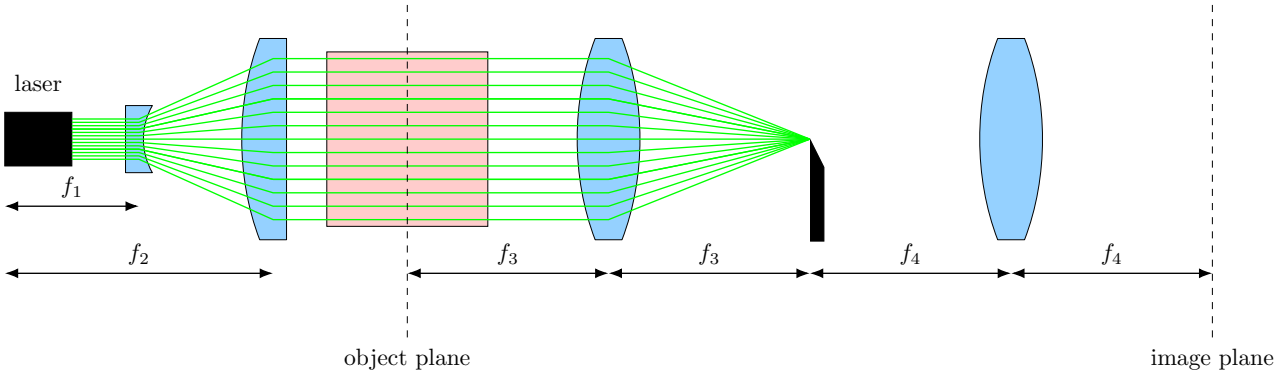

Figure 3.4.: Schlieren setup without object.

of plasma and rubidium vapor is wave length dependent. The first two lenses expand the beam of the laser to a larger diameter. This beam expander is followed by a conventional 4f-system. The focal length of lens 3 and lens 4 do not have to be equal. If they are different, we have magnification or demagnification. A razor blade at the position of the focal point of lens 3 is added with vertical position at the beam height. From ray optics perspective we will not see any signal at the image plane since we are blocking the rays. But due to diffraction and lens aberrations we are only obstructing half the focal spot and we will see a homogenous but reduced intensity at the image plane. The situation changes if we add our schlieren object to the setup. In general, this would be an arbitrary transparent object with a different refractive index than the surrounding medium.

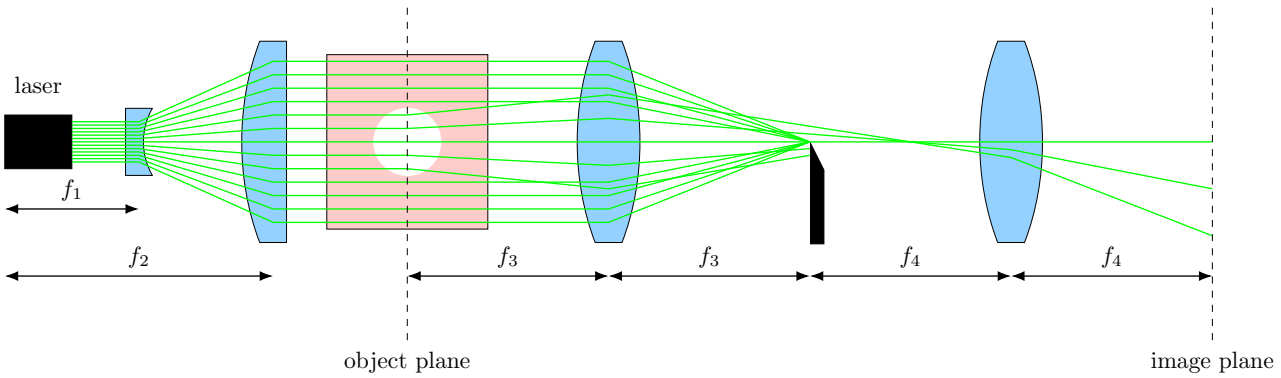

Figure 3.5.: Schlieren setup with plasma column (white) within rubidium vapor (red).

In Figure 3.5 we added the schlieren object to the setup. The plasma column is created by the ionizing laser within a long tube which contains rubidium vapor. Since we look sideways

through the tube we draw a quadratic cross section. Now our column deflects the rays in a well known manner. Depending on the refractive index of rubidium determined by the laser detuning frequency it will act as a focusing or defocusing lens. As we can see in the figure upwards deflected rays will be passing the razor blade above the edge. This later becomes the signal we want to analyze. In this case the radius of the plasma column would be the diameter (we also have to divide by the magnification) of the bright region at the image plane. The downwards deflected rays are fully blocked by the razor blade. We can only obtain the diameter but not the focal length, and therefore neither the refractive index, of the column. So this ray optics approach will give us only the diameter. Later we will see that a complete wave optics approach also reveals details about the focal length.

3.4. Shadowgraphy

A similar technique, which is also used for imaging objects with different refractive indices, is called shadowgraphy. In distinction to schlieren imaging we do not need a razor blade. Instead the deflection of the rays is directly projected onto the screen as seen in Figure 3.6. One requirement for accurate results is a small divergence of the laser beam. Depending on the laser wavelength our plasma column can act as a focusing lens. This is what we prefer in our experiments because the focal length determination of a focusing column is easier in comparison to a defocusing column. For a defocusing column one would need a relay imaging system to detect the virtual focal point. In Figure 3.7 we can see the sketch of the shadowgraphy setup with a focusing plasma column. From the distance to the focal point we can determine the focal length f_p.

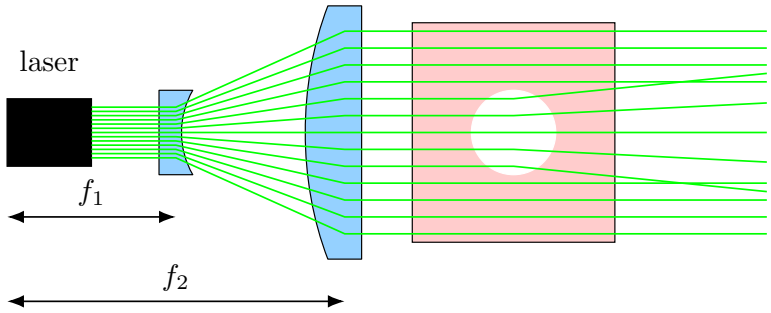

Figure 3.6.: Shadowgraphy setup with defocusing plasma column.

From the shadow of the target furthermore we can determine the diameter of the column $2R$.

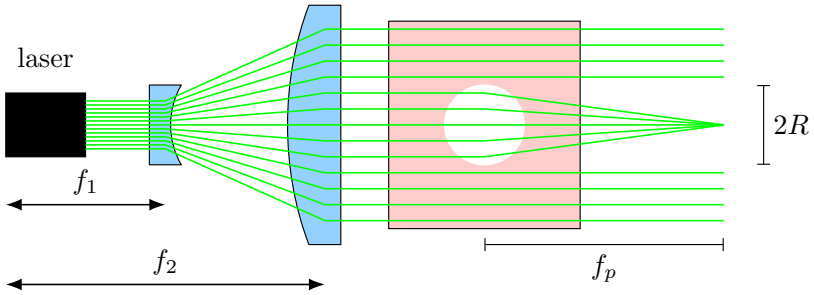

Figure 3.7.: Shadowgraphy setup with focusing plasma column.

From this chapter, we conclude that shadowgraphy is better than schlieren imaging because it reveals both the diameter and the focal length of the plasma column. However, in our theoretical simulations and experiments we will see that this conclusion neglects the important diffraction effects and therefore may only be true for a specific set of parameters.

4. Simulation Results

This chapter covers the simulation and theory results for the determination of the plasma column radius and the refractive index of rubidium vapor. All simulations are realized with `MATLAB` and based on Appendix A. Therefore, we always take diffraction of the razor blade and the targets into account but not diffraction of the optical system itself. This is not a problem since we use lenses with large diameter and therefore diffraction of them is negligible. At the beginning we introduce the two setups we use. Afterwards we will introduce our three targets and present the results. The `MATLAB` source code of the simulation can be found on GitHub [1].

4.1. Lens Setup

In the following we describe the theoretical model of the schlieren and the shadowgraphy setup.

Schlieren setup

Figure 4.2 shows the schlieren setup we use in our simulations.

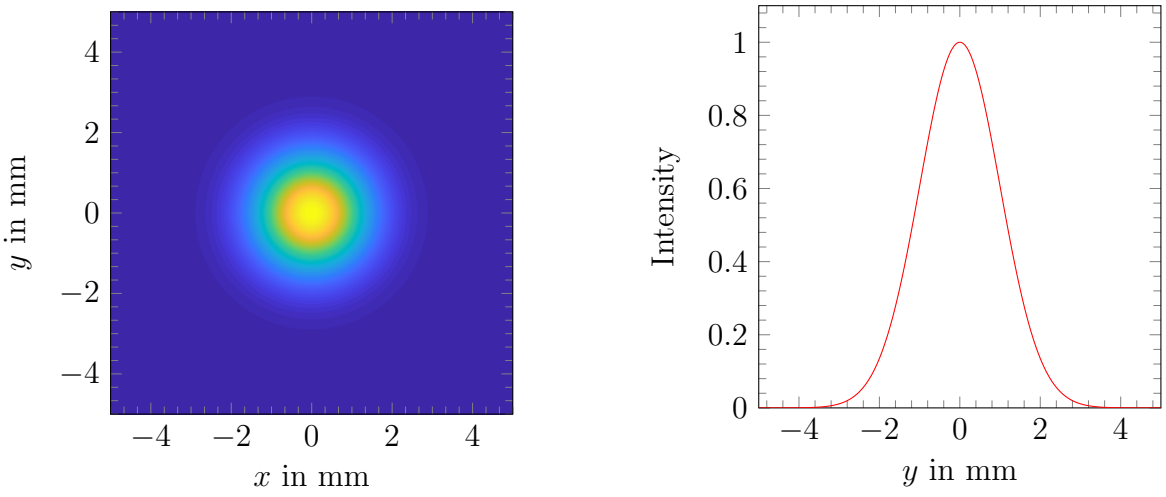

(a) Intensity distribution

(b) Lineout

Figure 4.1.: Intensity of the Gaussian beam with $\sigma_r = 2\,\text{mm}$.

[1] `https://github.com/roflmaostc/Schlieren-and-Shadowgraphy-Simulation`

In comparison to Figure 3.5 we removed the beam expander since we set the diameter of the laser in our source code directly. We assume that our laser beam has a Gaussian beam distribution in the electrical field:

$$g(x,y) = A \exp\left(-\frac{x^2+y^2}{\sigma_r^2}\right) \tag{4.1}$$

where σ_r is the standard deviation of the laser beam. In Figure 4.1 the intensity profile of the Gaussian beam is drawn. Note that we choose the electrical field according to Equation 4.1 and that the intensity is proportional to $|g(x,y)|^2$. This affects the standard deviation of the intensity profile. However, for our purpose it is not crucial that the laser has a Gaussian beam shape because all the results can be similarly approached with different beam shapes. The lens setup in Figure 4.2 is called a 4f-system. The object is placed exactly one focal length f_3 in front of the first lens. The distance between the first and second lens is $f_3 + f_4$ and finally the image plane is one focal length f_4 behind the second lens. This system fulfills the imaging condition [Gu00]. The numerical modelling of this setup is simple if we recap the results from Appendix A. We know that the electrical field one focal length behind the lens is just a Fourier

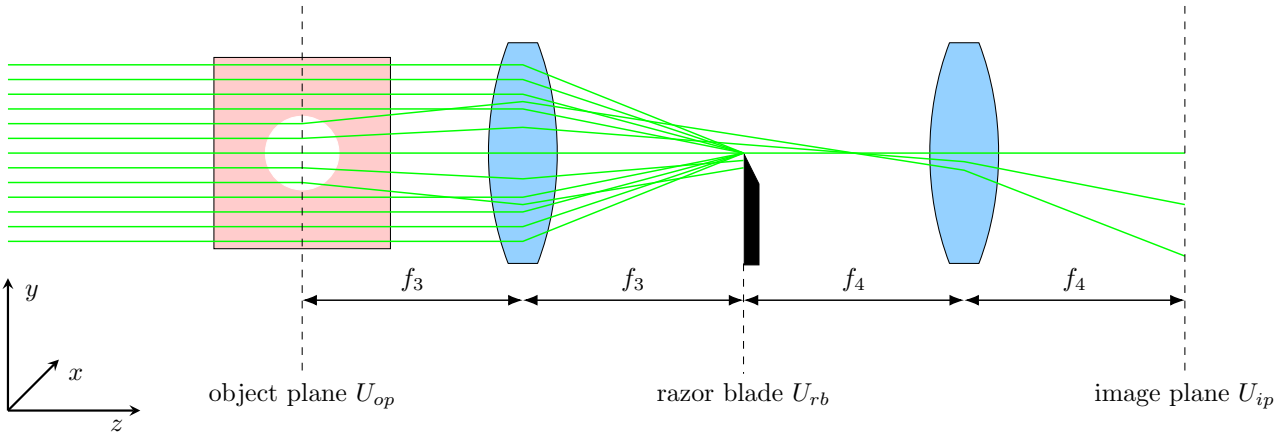

Figure 4.2.: Schlieren setup used for the simulations

transform of the electrical field one focal length in front of the lens. So the field in front of the razor blade is given by:

$$U_{rb}^{-}(x,y) = \frac{2\pi}{\lambda f_3}\,\mathcal{F}(U_{op})\left(\frac{k}{f_3}x, \frac{k}{f_3}y\right) \tag{4.2}$$

where f_3 is the focal length of the lens and k is the wave number. At the razor blade we cut half of the electrical field by our razor blade. This can be done with a modified 2D Heaviside step function:

$$\Theta(y) = \begin{cases} 0 & \text{for } y < 0 \\ 1 & \text{for } y \geq 0 \end{cases} \tag{4.3}$$

Using Θ we have a expression for U_{rb}^{+}:

$$U_{rb}^{+}(x,y) = \Theta(y) \cdot U_{rb}^{-}(x,y) \tag{4.4}$$

Finally, we can do a second Fourier transform to obtain the field given at U_{ip}:

$$U_{ip}(x,y) = \frac{2\pi}{\lambda f_4} \mathcal{F}(U_{rb}^{+}) \left(\frac{k}{f_4} x, \frac{k}{f_4} y \right) \tag{4.5}$$

The results of Equation 4.5 can not be obtained analytically anymore. To evaluate this we are going to use `MATLAB`. The physical description of how the object affects the electrical field U_{op} will be part of Section 4.2.

Shadowgraphy Setup

In Figure 4.3 the setup for the shadowgraphy imaging is shown. For that we do not need any lenses and consistently we assume a Gaussian beam spot which already has a larger diameter than our target. As explained in Section 3.4 we are using the property that the plasma column can act as a focusing lens if we choose a imaging laser wavelength in which the refractive index of the rubidium vapor is smaller than that of the plasma. U_{fp} can be expressed with a single

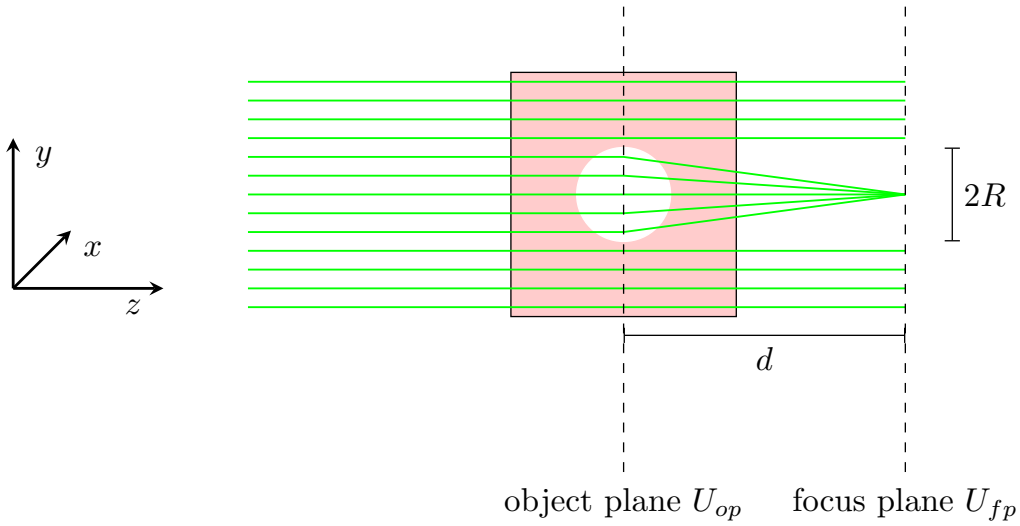

Figure 4.3.: Shadowgrapy setup used for the simulations

Fresnel propagation as derived in Section A.1. So our final field U_{fp} is given by the integral:

$$U_{fp}(x,y,d) = \frac{\exp(ikd)}{i\lambda} \int_{-\infty}^{\infty} \int_{-\infty}^{\infty} U_{op}(\xi,\eta) \frac{\exp\left(\frac{ik}{2d}\left((x-\xi)^2 + (y-\eta)^2\right)\right)}{d} \mathrm{d}\xi \mathrm{d}\eta \tag{4.6}$$

This integral can be evaluated numerically, see Section A.6.

4.2. Plasma Column

In this section we explain how we model the plasma column in our wave optics simulation. As mentioned in Appendix A we can only modify phase and amplitude in wave optics. Assuming

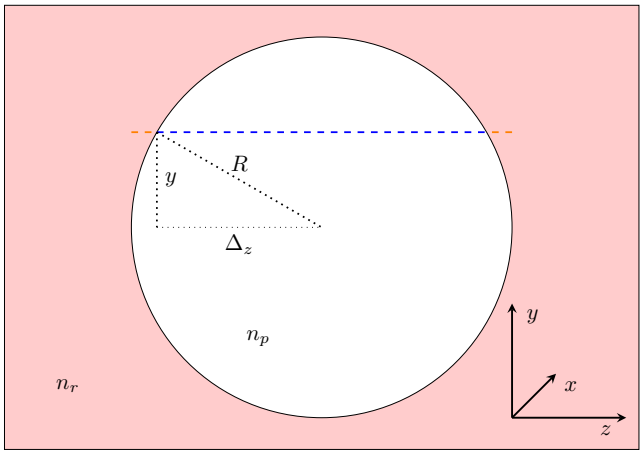

Figure 4.4.: Cross section of plasma column surrounded by rubidium vapor.

that our plasma column does not reflect a significant amount of light only the phase will be shifted during transition of our object. So our wave will simply undergo a phase shift which depends on the y-position. In x-direction we assume a column which is much longer than the extension of the laser beam. So we can derive Δ_z by using Pythagoras' theorem:

$$\Delta_z(y) = \sqrt{R^2 - y^2} \tag{4.7}$$

Δ_z is half of the distance propagated through the plasma. The whole distance is the dashed blue line. The distance propagated through rubidium vapor is the dashed orange line. The complete phase shift can be expressed with a piecewise function:

$$\Delta\Phi_{pc}(y) = \begin{cases} k_r \cdot 2R & \text{if } |y| > R \\ k_r \cdot (2R - 2 \cdot \Delta_z(y)) + k_p \cdot 2\Delta_z(y) & \text{if } |y| \leq R \end{cases} \tag{4.8}$$

where $k_r = \frac{2\pi n_r}{\lambda}$ and $k_p = \frac{2\pi}{\lambda}$. The first case is the constant phase shift due to the rubidium vapor. For waves passing through the column we subtract the distance which is not propagated in rubidium vapor and instead add the phase shift due to the plasma propagation. So our initial

electrical field U_{op} will be the laser beam multiplied with the phase shift due to the column:

$$U_{op}(x,y) = g(x,y) \cdot t_{pc}(x,y) = g(x,y) \cdot \exp\left(i \cdot \Delta\Phi_{pc}(y)\right) \tag{4.9}$$

Schlieren Imaging In Figure 4.5 we can see a simulated image of the plasma column using the schlieren setup.

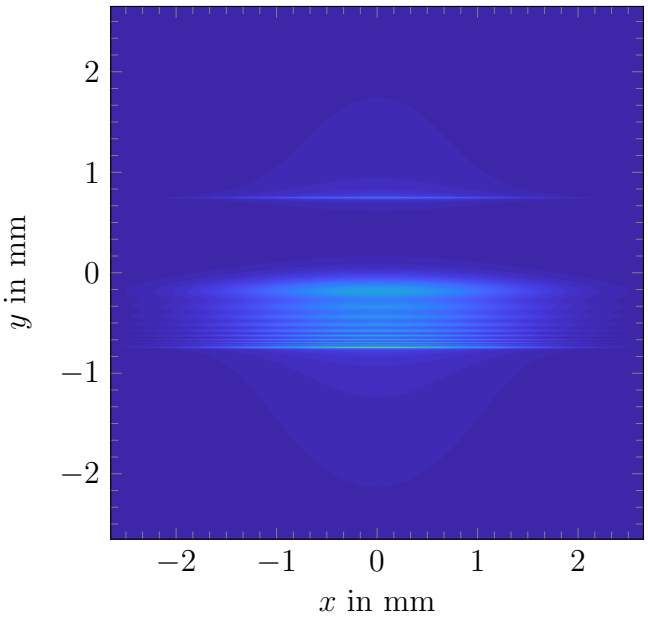

Figure 4.5.: Schlieren image of the plasma column target. $\sigma_r = 2\,\text{mm}$, $R = 0.75\,\text{mm}$, $n_r = 1.006$

We can identify a few characteristics. Roughly the top half has zero intensity and the bottom half a constant one. This can be explained by simple ray optics. A schematic ray trace is drawn in Figure 4.2.

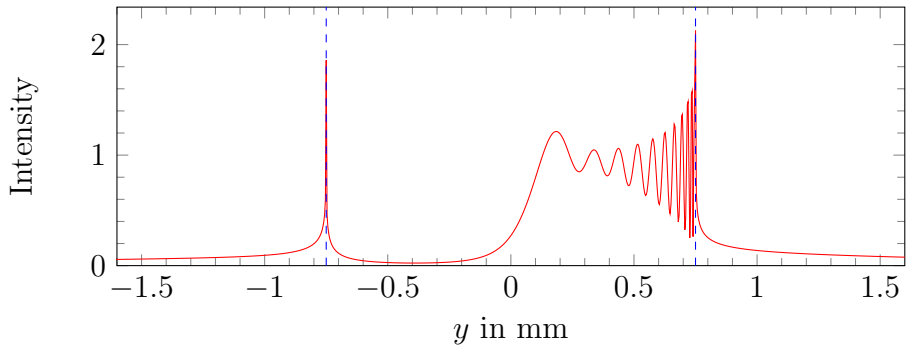

Figure 4.6.: Lineout at $x = 0\,\text{mm}$ of Figure 4.5

If we look closer, we can see an oscillating structure within the bright part. These are diffraction patterns induced by our single razor blade. The structure of the oscillation is dependent on

the laser wavelength, refractive index of the rubidium vapor, the y-position of the razor blade and the plasma column radius R. In contradiction to the ray optics model there is also some intensity at $y \approx 0.75\,\text{mm}$. This is generated due to diffraction bending light around the razor blade.

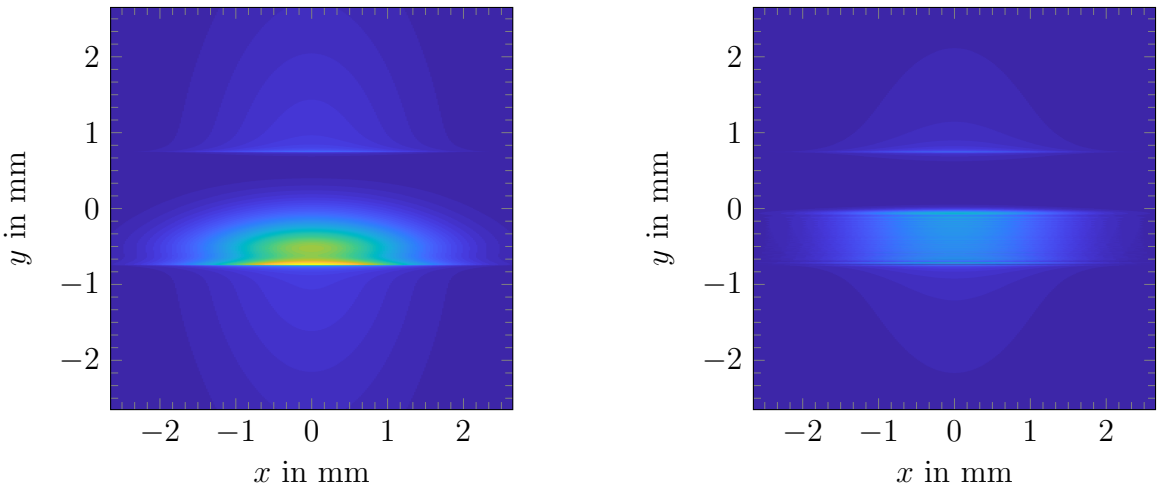

(a) $n_r = 1.0006$ (b) $n_r = 1.06$

Figure 4.7.: Dependency of the diffraction pattern on the refractive index of the rubidium vapor. $\sigma_r = 2\,\text{mm}$, $R = 0.75\,\text{mm}$.

In Figure 4.6 we can see the lineout at $x = 0\,\text{mm}$ of Figure 4.5. The determination of the diameter of the plasma column can be done my measuring the distance between the two peaks which are marked by the blue lines. The position of the peaks correspond to the plasma column radius. In Figure 4.7 we can see the change of the diffraction pattern if we vary the refractive index.

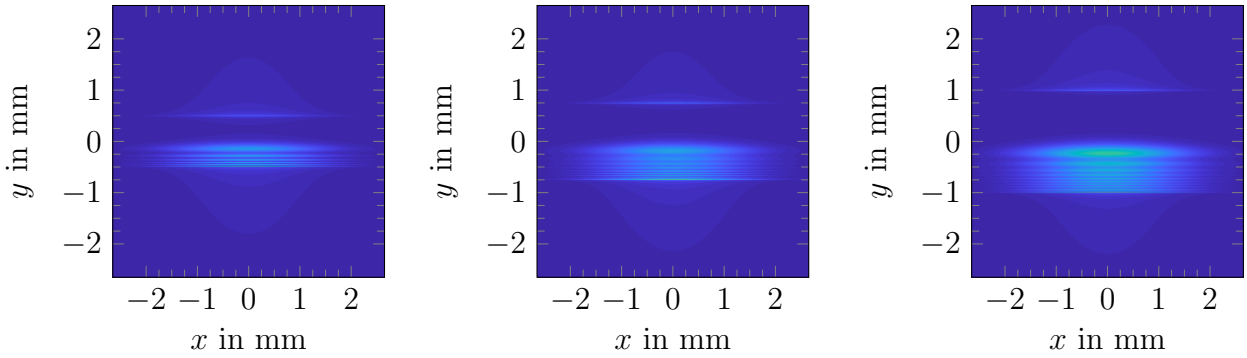

(a) $R = 0.5\,\text{mm}$ (b) $R = 0.75\,\text{mm}$ (c) $R = 1\,\text{mm}$

Figure 4.8.: Dependency of the diffraction pattern on the radius plasma column. $\sigma_r = 2\,\text{mm}$, $n_r = 1.006$.

We can also vary the diameter of the plasma column. The results of the variation can be seen in Figure 4.8. The main signal does not change a lot just the oscillating structure is extended by the same amount as the diameter is increased.

Shadowgraphy Figure 4.9 shows the simulation results of the plasma column target. The refractive index of rubidium is $n_r = 1 - 0.03$, the radius $R = 0.75\,\text{mm}$ which leads to an focal length of $f = 12.5\,\text{mm}$ according to Equation 3.6. We set the distance of the Fresnel propagation to $d = 12.5\,\text{mm}$ where we expect the focal point of the column, see Figure 4.3.

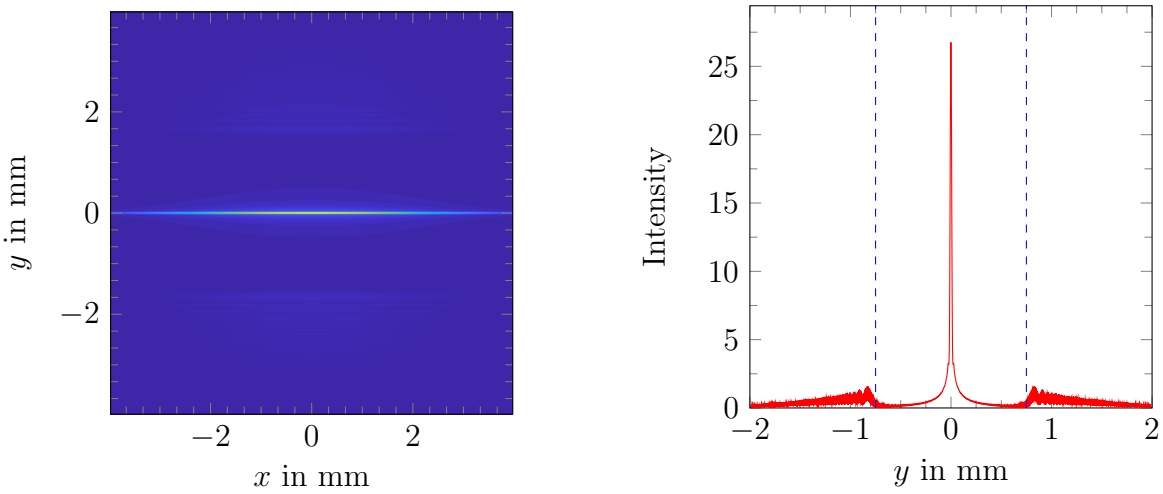

(a) Intensity distribution

(b) Cross section

Figure 4.9.: Shadowgraphy of the column with propagation distance behind the column $d = 12.5\,\text{mm}$. $\sigma_r = 2\,\text{mm}$, $R = 0.75\,\text{mm}$, $n_r = 1 - 0.03$

It shows that our column focuses the light which is passing through the column onto one line. So measuring the distance between the column and the focal spot gives us the focal length and therefore the refractive index. That way one can not detect the diameter of the column. Indeed we see a peak on the left and right in Figure 4.9b. But the blue dashed lines indicate the real diameter of the column. The visible peaks in the image are not the boundary of the column. The sub millimeter difference can be explained by diffraction effects which are induced by the small plasma column.
We also discovered in our simulations that for larger focal lengths of the plasma column the focal point is significantly placed in front of the focal length which is predicted by ray optics. The reason for this focus shift is the significant diffraction of that millimeter object. For a single slit the first maximum can be observed with a distance to the center x:

$$x \approx \frac{3\lambda}{2B} \cdot d \tag{4.10}$$

If we insert a millimeter object for the slit width B and a meter distance for the distance to the screen d, we will get the first maximum at $x \approx 1\,\text{mm}$. This rough estimation shows that diffraction influences our focusing behaviour of the lens. Therefore, we should choose a small focal length of the plasma column to prevent significant deviations due to diffraction.

4.3. Fuzzy Plasma Column

We can also realize a fuzzy plasma column where we do not have a sharp boundary between rubidium and plasma. To model a fuzzy edge we assume that we have a radial distribution of the wave number. Outside of r_o there is only rubidium vapor with wave number k_r. In the transition between r_o and r_i we do a linear interpolation between k_r and the wave number of plasma k_p. Within the inner radius r_i there is only plasma present.

$$\Delta k_{fpc}(z,y) = \begin{cases} k_r & \text{if } \sqrt{z^2+y^2} \geq r_o \\ m \cdot \sqrt{z^2+y^2} + t & \text{if } r_o > \sqrt{z^2+y^2} \geq r_i \\ k_p & \text{if } \sqrt{z^2+y^2} < r_i \end{cases} \tag{4.11}$$

For the linear interpolation the parameters are $m = \frac{k_r - k_p}{r_o - r_i}$ and $t = k_r - m \cdot r_o$. Figure 4.10 shows the fuzzy plasma column. To model the phase shift we have to look at the three stages of propagation. The first one is the dashed orange line with a distance in rubidium of $2r_o - 2\Delta_1$.

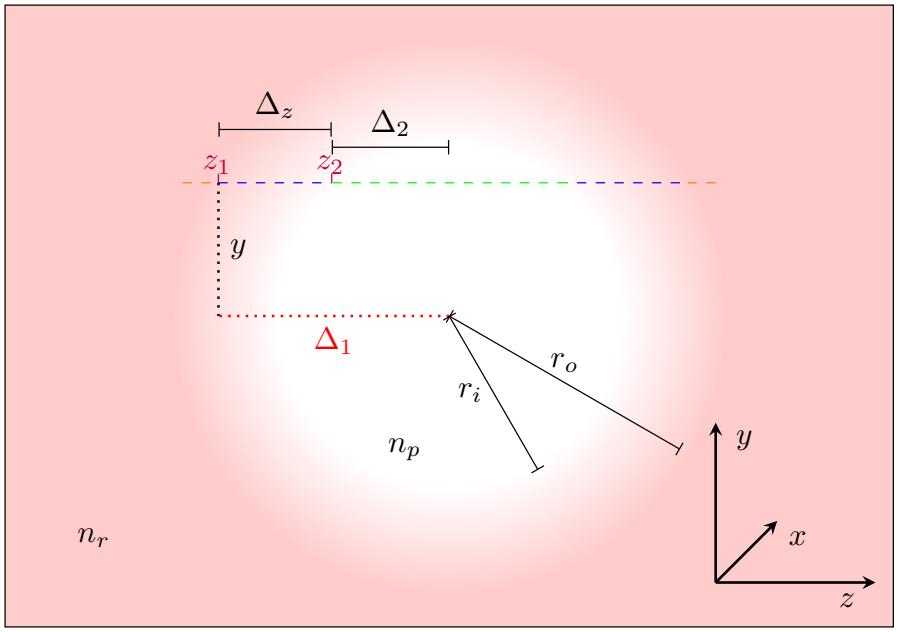

Figure 4.10.: Cross section of fuzzy plasma column.

Therefore, the phase shift due to this pure rubidium layer is:

$$\Delta\Phi_{fpc,1}(y) = k_r \cdot (2r_o - 2\Delta_1(y)) \tag{4.12}$$

where $\Delta_1(y) = \sqrt{r_o^2 - y^2}$. Note that a factor of 2 is multiplied since we have the phase shift first on the entering side and second on the exiting side. The phase shift for the plasma propagation (green dashed line) is simply given by:

$$\Delta\Phi_{fpc,3}(y) = 2 \cdot k_p \cdot \Delta_2(y) \tag{4.13}$$

where $\Delta_2(y) = \sqrt{r_i^2 - y^2}$. The phase shift through the fuzzy part (blue dashed line) between r_o and r_i is not a simple multiplication since we do not have a constant wave number. The phase shift for an infinitesimal $\mathrm{d}z$ would be:

$$\mathrm{d}(\Delta\Phi_{fpc,2}(z,y)) = (m \cdot \sqrt{z^2 + y^2} + t)\,\mathrm{d}z \tag{4.14}$$

We can integrate this from z_1 to z_2 and multiply it by 2 to obtain the full phase shift within the fuzzy part:

$$\Delta\Phi_{fpc,2}(y) = 2 \cdot tz + mz\sqrt{z^2 + y^2} + my^2 \log\left(z + \sqrt{z^2 + y^2}\right)\Big|_{z_1}^{z_2} \tag{4.15}$$

where $z_1 = \Delta_1(y)$ and $z_2 = \Delta_2(y)$. The full phase shift can be expressed by:

$$\Delta\Phi_{fpc}(y) = \begin{cases} k_r \cdot 2r_o & \text{if } |y| \geq r_o \\ \Delta\Phi_{fpc,1}(y) + \Delta\Phi_{fpc,2}(y) & \text{if } r_o > |y| \geq r_i \\ \Delta\Phi_{fpc,1}(y) + \Delta\Phi_{fpc,2}(y) + \Delta\Phi_{fpc,3}(y) & \text{if } |y| < r_i \end{cases} \tag{4.16}$$

The final field is:

$$U_{op}(x,y) = g(x,y) \cdot t_{fpc}(x,y) = g(x,y) \cdot \exp\left(i \cdot \Delta\Phi_{fpc}(y)\right) \tag{4.17}$$

Schlieren In Figure 4.11 we can see the schlieren simulation of the fuzzy plasma column. For r_i we set $0.7 \cdot r_o$. The main difference between Figure 4.11b and Figure 4.6 is the peak height. Especially the left peak is decreased roughly by a factor of 3.

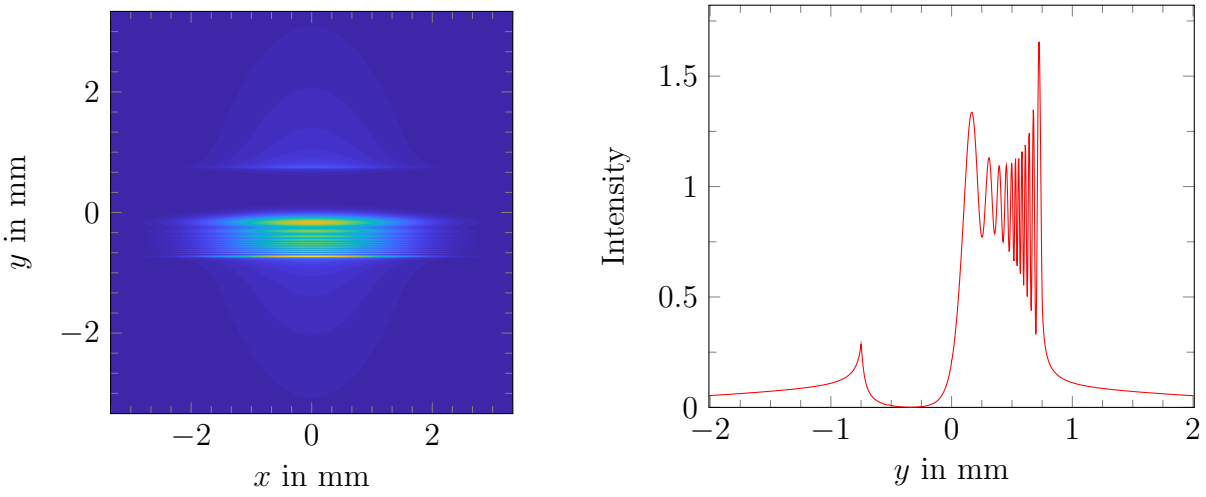

(a) Intensity distribution (b) Lineout

Figure 4.11.: Schlieren image of the fuzzy plasma column target. $\sigma_r = 2\,\text{mm}$, $r_o = 0.75\,\text{mm}$, $r_i = 0.7r_o$, $n_r = 1.006$.

In experiments at AWAKE we expect that there will be a fuzzy plasma column which could mean that the size is not as clearly visible as maybe expected with an ideal plasma column.

Shadowgraphy In Figure 4.12 we use the same fuzzy plasma column for our shadowgraphy setup.

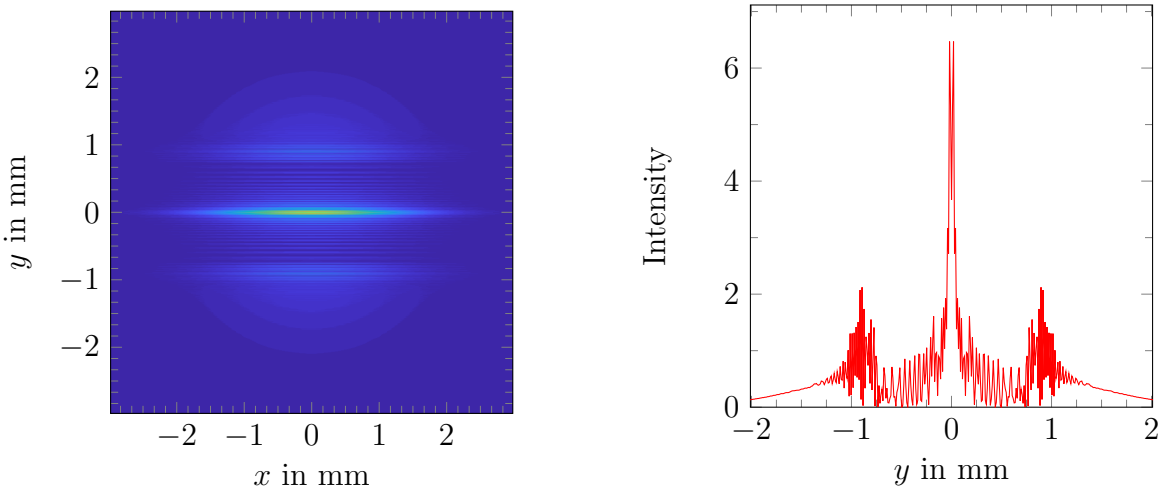

(a) Intensity distribution (b) Lineout

Figure 4.12.: Schlieren image of the fuzzy plasma column target. $\sigma_r = 2\,\text{mm}$, $R = 0.75\,\text{mm}$, $n_r = 1.006$

What we observe is that the edges of the plasma column smear even more out in comparison to Figure 4.9. This is reasonable since we try to model the plasma column in such a way that there

is no sharp column boundary. The focal line is also affected by the fuzzy edge and is indeed different to the one of the perfect plasma column since the derivation of focal lengths works only if one has perfect boundaries. An explicit equation for the focal length of a fuzzy plasma column is not given and we are not sure if it is possible to derive one.

4.4. Cylindrical Lens

The first target we use in the experiments is a cylindrical lens with an extension in x-direction that is much longer than the width of our laser beam whereas it is smaller in y-direction. Cylindrical lens implies that there is only a curvature along the x-axis but not along the y-axis. Therefore, the optical property of focusing light is the same. Neglecting intensity loss we can describe the phase shift similar to Equation A.9:

$$t_{cl}(x,y) = \begin{cases} 1 & \text{if } |y| > h/2 \\ \exp\left(-i\,\frac{k}{2f}\,y^2\right) & \text{if } |y| \leq h/2 \end{cases} \tag{4.18}$$

We need to divide the transmission function into two parts. One part is the light bypassing above or below the lens height h. The second case describes the wave passing through the object. Similar to before the electrical field is:

$$U_{op}(x,y) = g(x,y) \cdot t_{cl}(x,y) \tag{4.19}$$

Schlieren Imaging For the simulation of the cylindrical lens we choose a focal length which is identical to that of the plasma column. Inserting the parameters into Equation 3.6 we get a value of $f = -62.5\,\text{mm}$. This is what we choose for our ideal cylindrical lens. The result is shown in Figure 4.13a. Again the diameter of the lens is clearly visible by the bright edges at the top and bottom and the diffraction pattern looks also similar to the plasma column simulation. However, on the bottom edge of Figure 4.13a are less oscillations than in Figure 4.5. This is due to the fact that the lens has a perfect focal point. In contrast the plasma column is strongly affected by spherical aberrations. Spherical aberrations are lens errors induced by lenses which do not have a small size in comparison to the radius of curvature. So the assumption of an ideal lens is only valid for the center region of the column. Since we are using the whole diameter of the plasma column this is not the case. In Figure 4.13b we choose the same focal length but instead with focusing behaviour. We see that the pattern is vertically flipped which can be explained by ray optics due to the focusing property of the lens exactly the other half is cut off by the razor blade.

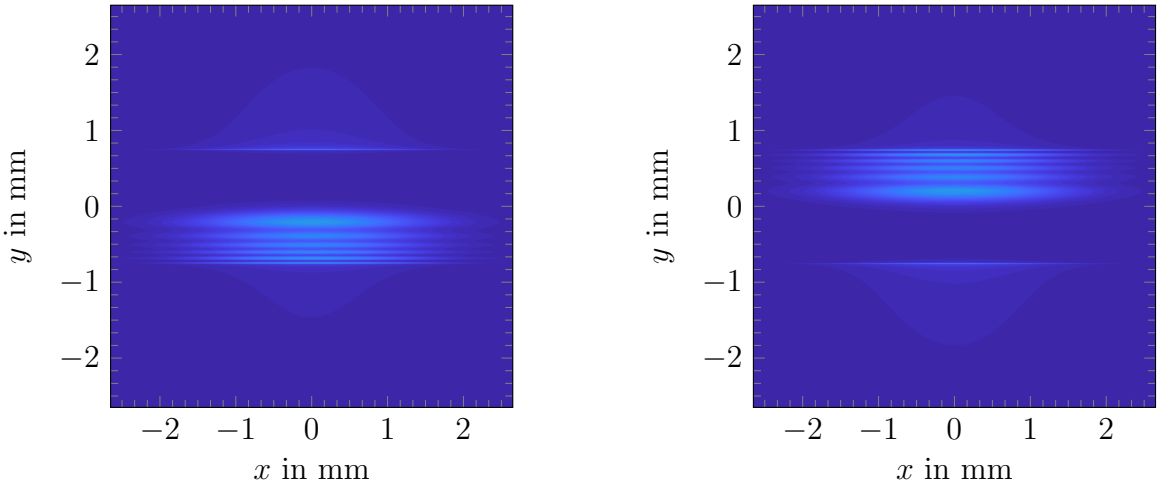

(a) $f = -62.5\,\text{mm}$ (b) $f = 62.5\,\text{mm}$

Figure 4.13.: Schlieren image of the lens target. $\sigma_r = 2\,\text{mm}$, $R = 0.75\,\text{mm}$.

Shadowgraphy In Figure 4.14 the results of the shadowgraphy simulation can be seen. Figure 4.14b shows that the minimum of the intensity is roughly at $\pm 0.75\,\text{mm}$ corresponding to the diameter of the cylindrical lens. The object is the cylindrical lens with a focal length of $f = 62.5\,\text{mm}$. The propagation is done with a Fresnel propagation over a distance of $d = 40\,\text{mm}$.

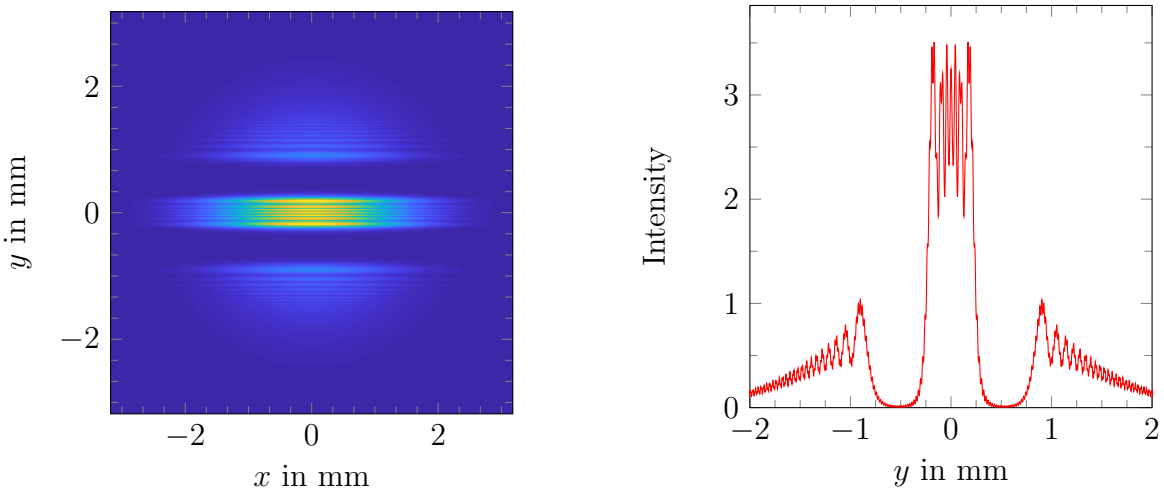

(a) Intensity distribution (b) Lineout

Figure 4.14.: Shadowgraphy of the lens with propagation distance behind lens $d = 40\,\text{mm}$. $\sigma_r = 2\,\text{mm}$, $R = 0.75\,\text{mm}$, $f = 62.5\,\text{mm}$.

We expect that all light that went through the cylindrical lens will be focused onto a line 62.5 mm behind the target. Since in this figure we choose a smaller distance we are not at this point. But we see that everything within 0.75 mm lens radius is focused together.

In Figure 4.15 we show the propagation until the focal plane of the target. We see a clear separation of the focused light and the light which bypasses the cylindrical lens. However, due to the Fresnel propagation we have diffraction effects which smear out the sharp edges of the cylindrical lens and air. Also in Figure 4.15b we can not detect the edge precisely.

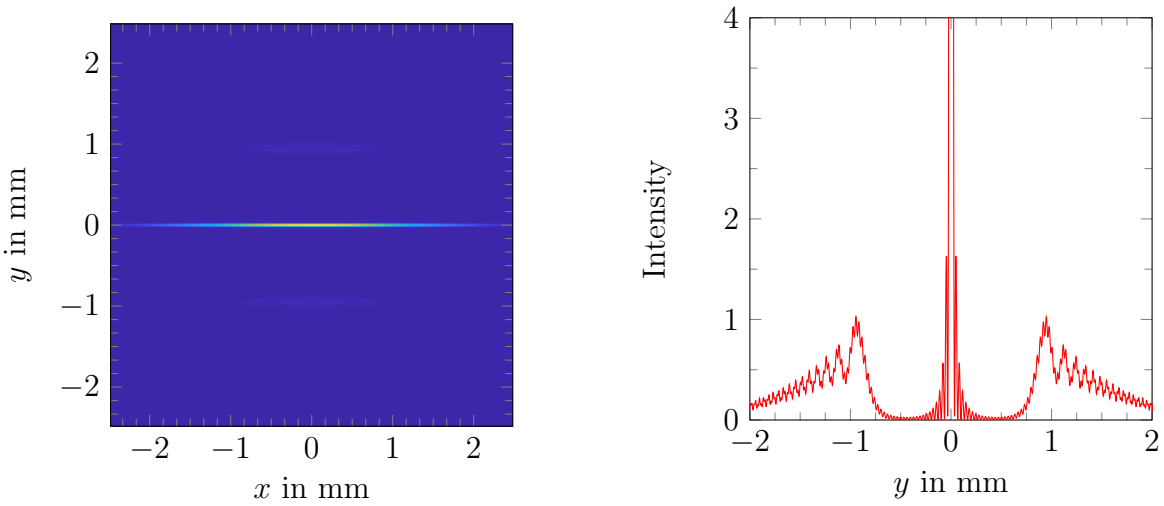

(a) Intensity distribution

(b) Lineout

Figure 4.15.: Shadowgraphy of the lens with propagation distance behind lens $d = 62.5\,\text{mm}$. $\sigma_r = 2\,\text{mm}$, $R = 0.75\,\text{mm}$, $f = 62.5\,\text{mm}$.

As conclusion one can say that by using shadowgraphy the edges of a cylindrical lens can be detected but with a smaller precision as in comparison to the schlieren setup. However, one can determine the focal length of the cylindrical lens.

4.5. Glass Capillary

Our second target is a glass capillary. In Figure 4.16 we can see the cross section of the glass capillary. To calculate the phase shift we derive Δ_z. Similar to before it is:

$$\Delta_1(y) = \sqrt{r_o^2 - y^2} \tag{4.20}$$

$$\Delta_2(y) = \sqrt{r_i^2 - y^2} \tag{4.21}$$

And therefore we obtain:

$$\Delta_z(y) = \Delta_1(y) - \Delta_2(y) = \sqrt{r_o^2 - y^2} - \sqrt{r_i^2 - y^2} \tag{4.22}$$

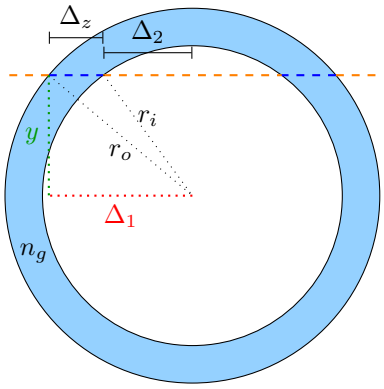

Figure 4.16.: Cross section of the glass capillary

Now we can express the phase shift as a piecewise function:

$$\Delta\Phi_{gc}(y) = \begin{cases} 2r_o k & \text{if } |y| \geq r_o \\ 2(r_o - \Delta_1(y))k + 2\Delta_1(y)k_g & \text{if } r_i > |y| \geq r_o \\ 2(r_o - \Delta_z(y))k + 2\Delta_z(y)k_g & \text{if } |y| < r_i \end{cases} \tag{4.23}$$

with $k = \frac{2\pi}{\lambda}$, $k_g = \frac{2\pi n_g}{\lambda}$ and n_g the refractive index of glass. So the final field is given by:

$$U_{op}(x, y) = g(x, y) \cdot t_{gc}(x, y) = g(x, y) \cdot \exp\left(i \cdot \Delta\Phi_{gc}(y)\right) \tag{4.24}$$

Schlieren Imaging In order to have similar optical properties, we choose a glass capillary

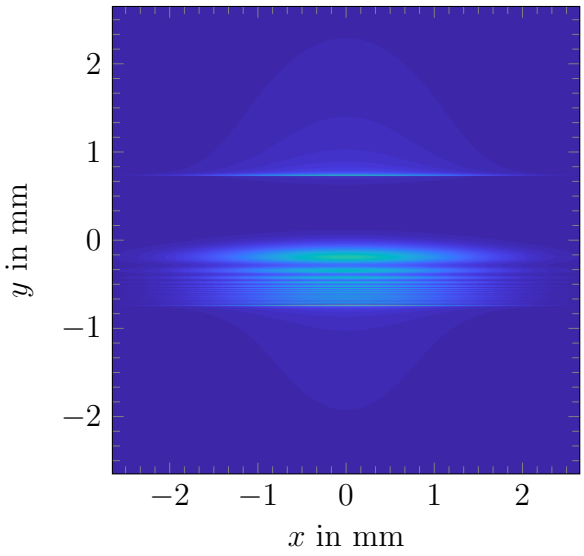

Figure 4.17.: Schlieren image of the glass capillary target. $\sigma_r = 2\,\text{mm}$, $r_i = 0.75\,\text{mm}$, $r_o = 0.7412\,\text{mm}$.

which has the same diameter $2 \cdot r_o = 1.5\,\text{mm}$ and an inner radius r_i leading to the same focal length of 62.5 mm using Equation 3.11. Hence, the value for r_i is 0.7412 mm. The result is shown in Figure 4.17. The diameter is as in the previous two targets clearly visible. The diffraction pattern at the bottom is similar to the one of the plasma column but not identical because the spherical aberrations are different.

Shadowgraphy As the last simulation we are doing the shadowgraphy with the glass capillary. For the glass capillary we use $r_o = 0.75\,\text{mm}$ and $r_i = 0.7444\,\text{mm}$ leading to an equivalent focal length of $-100\,\text{mm}$. Since the capillary acts defocusing we do not see a focused line using the setup from Figure 4.3. Instead the light passing through the capillary is spread from the center. To see the virtual focal line at $-100\,\text{mm}$ we need to use a relay imaging system in practice. In our simulation we can simply set a negative distance for the Fresnel propagation.

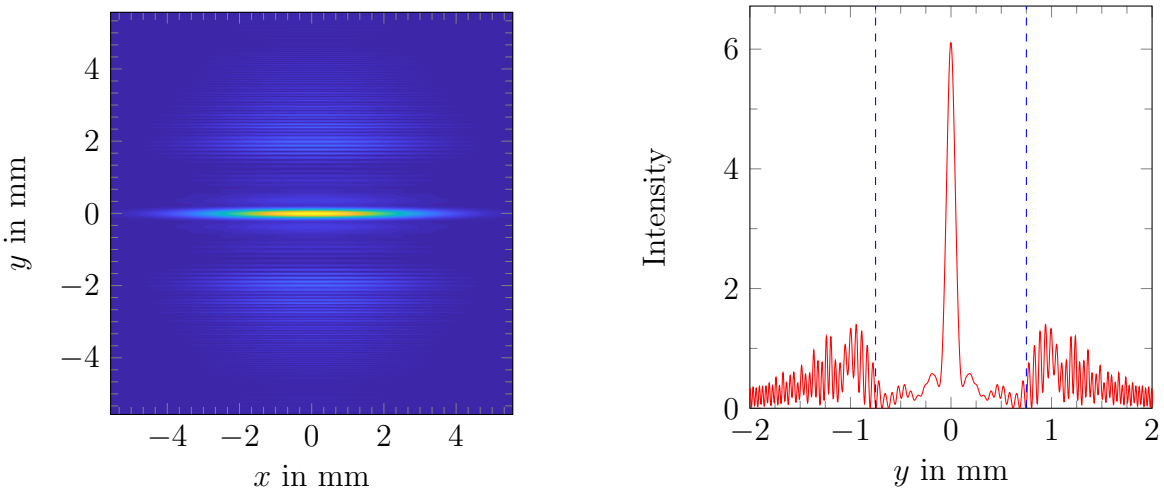

(a) Intensity distribution

(b) Cross section

Figure 4.18.: Shadowgraphy of the capillary with propagation distance in front of the capillary at $d = -100\,\text{mm}$. $\sigma_r = 2\,\text{mm}$, $r_o = 0.75\,\text{mm}$, $r_o = 0.7444\,\text{mm}$

Due to the diffraction effects one can not detect the boundary of the capillary precisely. In our experiments we are going to use larger capillaries where it is easier to detect the boundaries.

5. Experimental Results and Comparison with Simulation

In our last chapter we are going to analyze the experimental results of the cylindrical lens and two different glass capillaries. The latter behaves more like the plasma column because it is similarly affected by spherical aberrations and irregularities of the manufacturing process.

5.1. Experimental Imaging

Our experimental setup is given by Figure 3.5. For the laser source we have got two different possibilities.

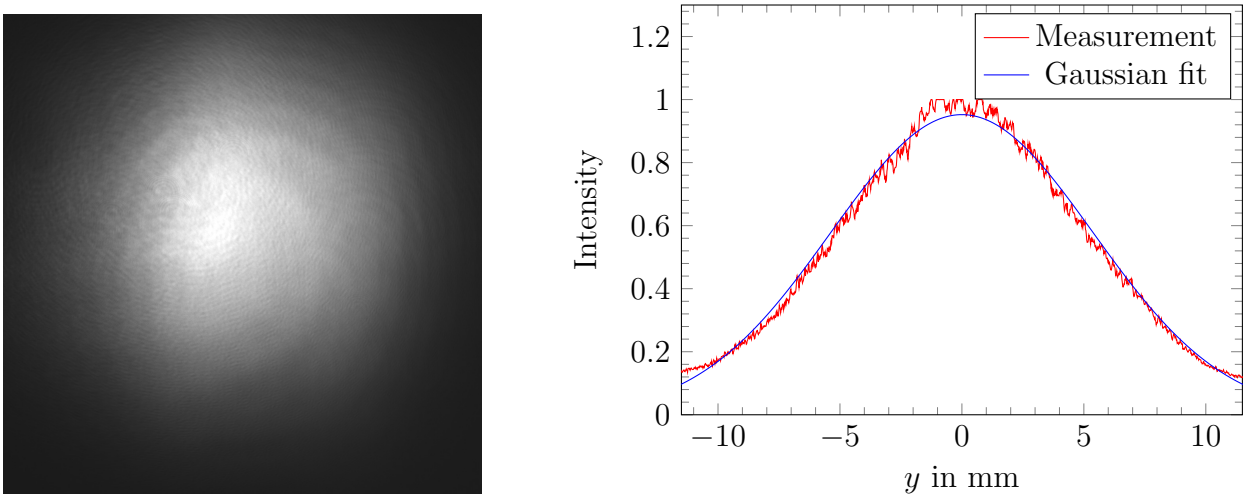

(a) Image taken with camera

(b) Lineout with a fitted Gaussian curve

Figure 5.1.: Image of the HNL100L laser beam.

The first one is the HNL100L[1] with a wavelength of 632.8 nm. This laser has approximately a Gaussian spot as seen in Figure 5.1. Our second laser diode is a CPS532-C2 [2] with 532 nm

[1] https://www.thorlabs.de/thorproduct.cfm?partnumber=HNL100L&pn=HNL100L#ad-image-0
[2] https://www.thorlabs.de/thorproduct.cfm?partnumber=CPS532-C2

wavelength. In comparison to the HNL100L the intensity distribution is not Gaussian and one can clearly see diffraction rings from the laser itself. Our camera is the Basler acA1920-155um [3] with a pixel size of 5.86 µm.

5.2. Cylindrical Lens

First, we discuss the measurements taken with the schlieren setup and afterwards that one taken with the shadowgraphy setup.

5.2.1. Schlieren Imaging

CPS532-C2 Laser The first images are taken with the cylindrical lens. For the cylindrical lens we choose a focusing lens with a focal length of 150 mm, a height of (12.38 ± 0.02) mm and a width of 25 mm. We set a size of the laser spot which is larger in the y direction but smaller in x direction. The used lenses for the setup are $f_1 = -100$ mm, $f_2 = 300$ mm, $f_3 = 500$ mm and $f_4 = 250$ mm. In Figure 5.2 experimental results can be seen. Figure 5.2a shows multiple diffraction patterns.

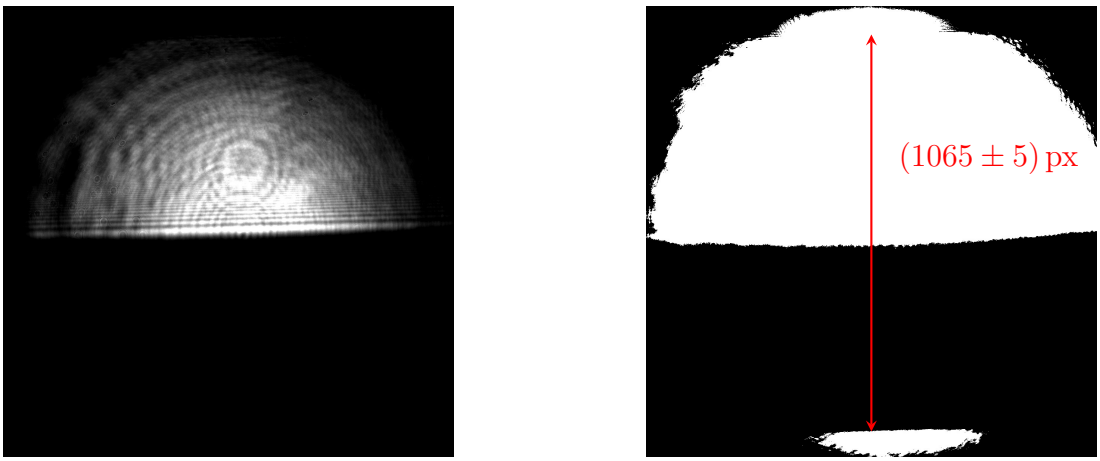

(a) With visible diffraction pattern (b) Threshold image

Figure 5.2.: Schlieren image of the cylindrical lens taken with CPS532-C2 laser.

The circular pattern and the large spot above the edge is created by the laser diode itself. We can find a diffraction pattern generated by the razor blade and the object, which is horizontal and central of the image. The diameter can also be detected. For that purpose we use Figure 5.2. We can count (1065 ± 5) px in diameter which is a length of (12.48 ± 0.06) mm. The transformation

[3] https://www.baslerweb.com/en/products/cameras/area-scan-cameras/ace/aca1920-155um/

between pixels and millimeters is done with multiplication of the number of pixels with pixel size and the magnification factor of f_4/f_3. The measured diameter is in good accordance with the given diameter of $(12.38 \pm 0.02)\,\mathrm{mm}$. For detecting the focal length of the cylindrical lens we are going to use the HNL100L since the laser spot is free of diffraction rings. This will remove some noise which is currently present.

HNL100L Laser For this laser we had to adapt the focal length of the lenses to fit everything appropriately on the sensor. The values are $f_1 = -100\,\mathrm{mm}$, $f_2 = 500\,\mathrm{mm}$, $f_3 = 500\,\mathrm{mm}$ and $f_4 = 250\,\mathrm{mm}$. Figure 5.3a shows the recorded image of the cylindrical lens placed at the object plane without a razor blade. Fulfilling imaging condition we expect to see no effect of the object since our lens is transparent. However, due to reflectivity and not perfect edges of the lens we can see the edges of the object.

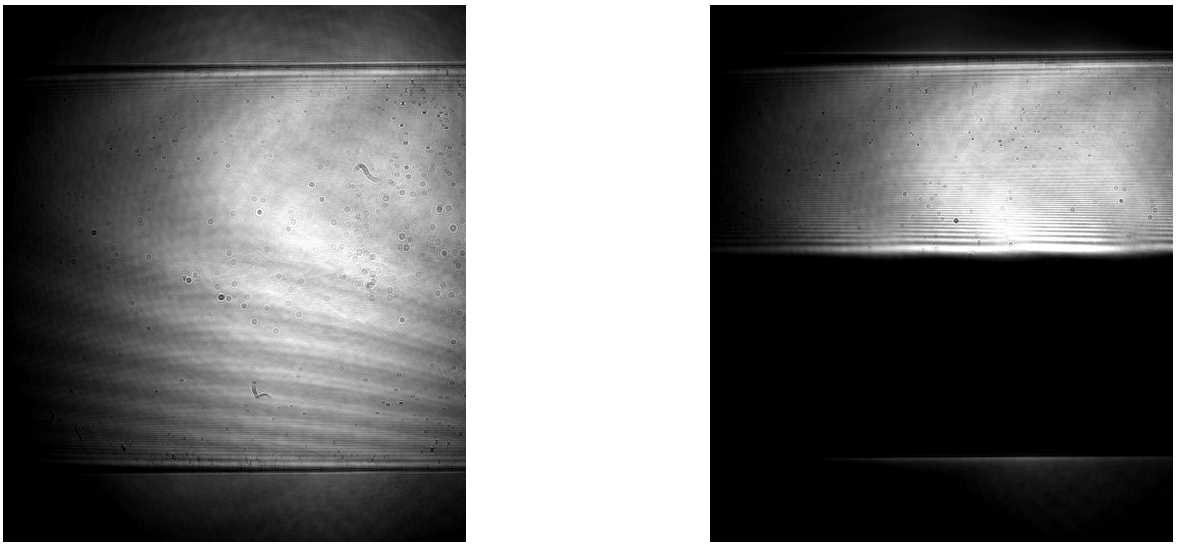

(a) Without razor blade (b) With razor blade

Figure 5.3.: Schlieren images of the cylindrical lens taken with HNL100L.

Additionally, we can see some sloped stripes, potentially from reflections within the cylindrical lens. The razor blade was added to the system in Figure 5.3b. Now we can detect the diameter of the object without relying on the previously described effects. Figure 5.4 shows that the distance between the left and right peak is $(1058 \pm 2)\,\mathrm{px}$ or $(12.40 \pm 0.02)\,\mathrm{mm}$. Within the error range the value of (12.38 ± 0.02) and this fit together.

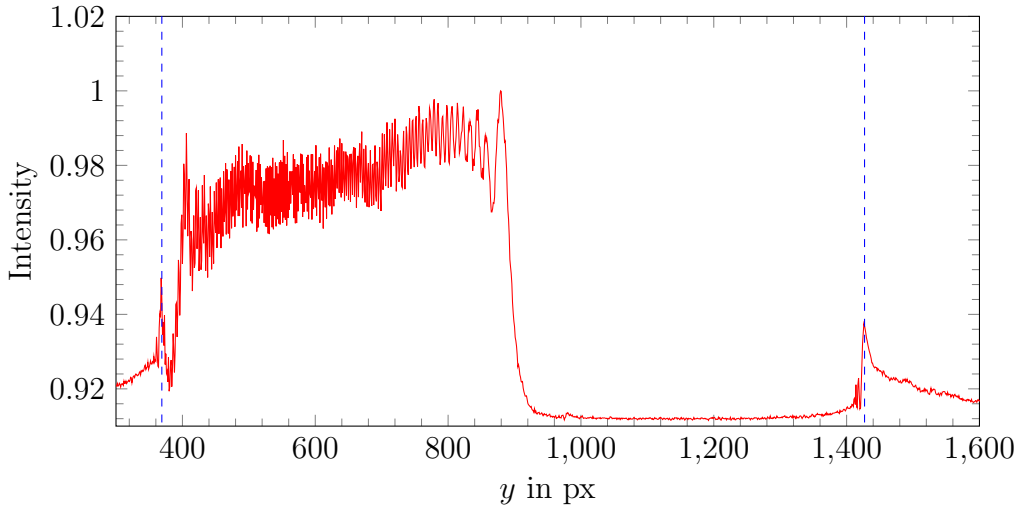

Figure 5.4.: Lineout of Figure 5.2.

5.2.2. Shadowgraphy Imaging

The shadowgraphy image of the cylindrical lens in Figure 5.5 is taken with the setup from Figure 3.7. Instead of placing the imaging sensor one focal length f_p behind the cylindrical lens we use a relay imaging system to demagnify the image to fit the signal on the sensor. On the left hand side in Figure 5.5a we set a short exposure time to confirm that we have a bright focused region. Due to the limited dynamic range of the camera we do not see the edges. To solve this we set a long exposure time in Figure 5.5b. Consequently, the center is overexposed but we can detect the edges of the object.

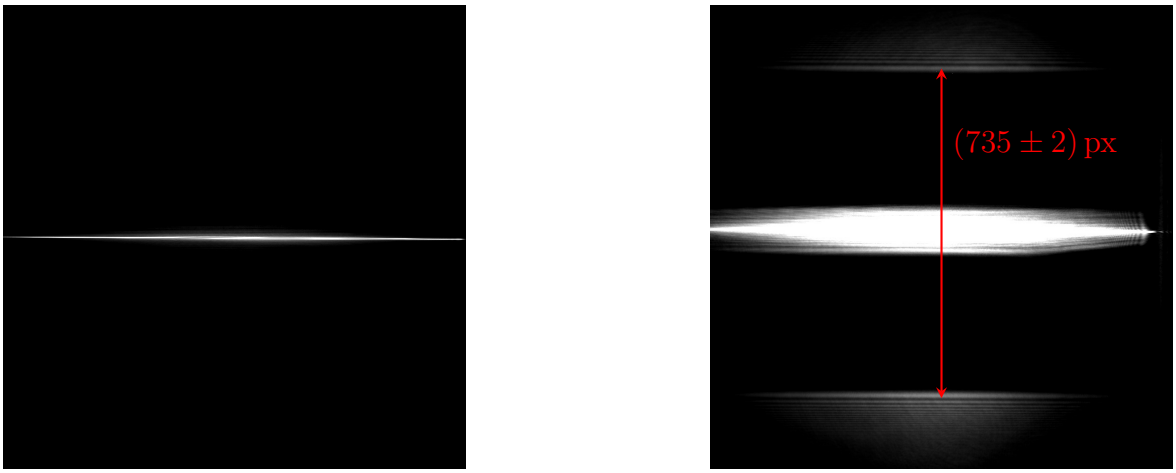

(a) Short exposure time

(b) Long exposure time

Figure 5.5.: Shadowgraphy image of the cylindrical lens taken with HNL100L.

We expect that the light which passes through the target will be focused on one line. Analyzing the shadow gives us (735 ± 2) px distance between the edges or equivalently (12.87 ± 0.04) mm. The diameter is due to diffraction larger than expected as we mentioned in Figure 4.18. Additionally, there is an error due to inaccurate collimation of the laser beam, estimated to be approximately 0.08 mm. The focal length of the target is $f_p = (150 \pm 5)$ mm and is confirmed with this shadowgraphy setup.

5.3. Glass Capillary

We also perform the previous measurements on glass capillaries. For this Hilgenberg[4] manufactured glass capillaries in two different sizes. We measured the outer radius of the capillary using a micrometer screw. The value we obtain is $r_{o,1} = (2.065 \pm 0.020)$ mm. For the wall thickness and therefore for the inner radius $r_{i,1} = 2.00$ mm we take the value of the manufacturer.
The second capillary has a measured radii of $r_{o,2} = (3.00 \pm 0.02)$ mm and $r_{i,2} = 2.95$ mm. Hilgenberg states for both radius values a error of 0.1 mm. Obviously, this can not be the real error. Therefore, we set the error to 0.02 mm which is what we can at least ensure for the outer radius. The refractive index for both capillaries is listed with $n = 1.473$ for a wavelength of 587.6 nm. According to Equation 3.11 the focal length of the first capillary is $f_{cp,1} = (-66 \pm 30)$ mm and that of the second one is $f_{cp,2} = (-186 \pm 100)$ mm. Since our focal length depends on the difference between the two radii and the error in the radii is large, the error in the focal length is large.

5.3.1. Schlieren Imaging

To fit the capillaries on the sensor we choose the following focal lengths for the schlieren setup: $f_1 = -100$ mm, $f_2 = 300$ mm, $f_3 = 500$ mm and $f_4 = 250$ mm. We use the HNL100L laser in our further experiments. The results of the experiment are shown in Figure 5.6.

[4] https://www.hilgenberg-gmbh.de/innovative-glasprodukte/

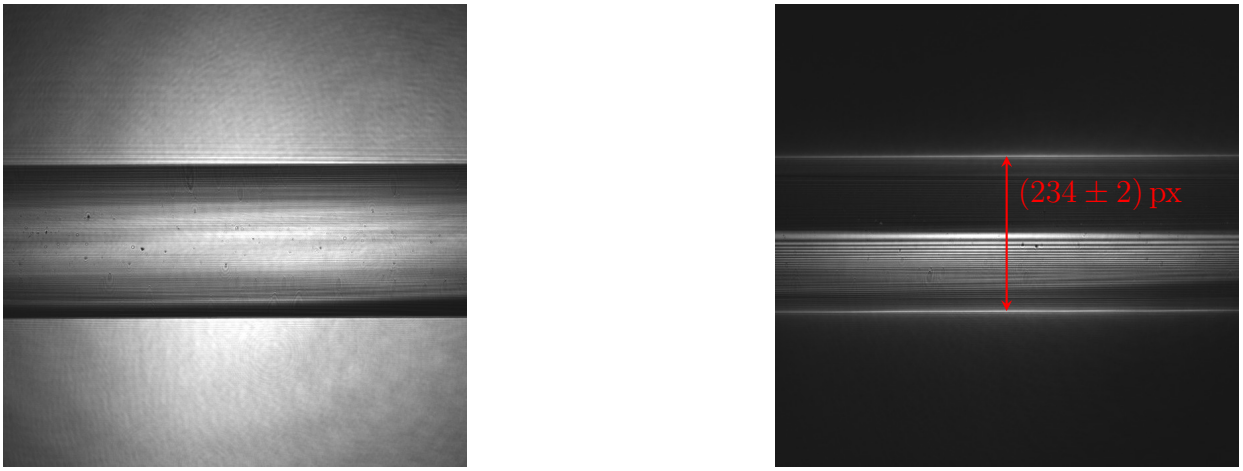

(a) Without razor blade

(b) With razor blade

Figure 5.6.: Schlieren image of the smaller glass capillary ($r_{o,1} = 2.065\,\text{mm}$, $r_{i,1} = 2\,\text{mm}$) taken with HNL100L

In Figure 5.7 we can see the simulated capillary of Figure 5.6. Qualitatively they look similar. For a closer investigation we can see a direct comparison of the lineout of experiment and

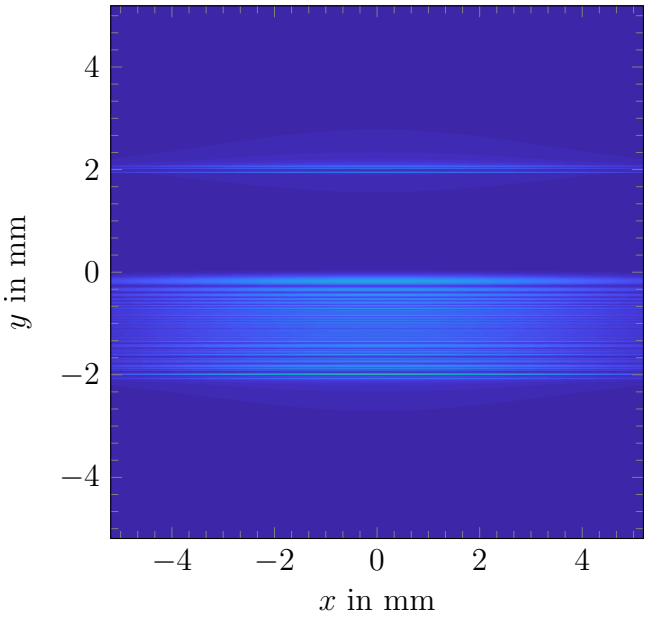

Figure 5.7.: Simulated Schlieren image of the smaller glass capillary ($r_{o,1} = 2.065\,\text{mm}$, $r_{i,1} = 2\,\text{mm}$)

simulation in Figure 5.8. The main difference is the central peak which is shifted with respect to the experimental peak. This is not a significant discrepancy between theory and experiment since the peak position depends on many parameter like razor blade position which are difficult

to control in the experiment.

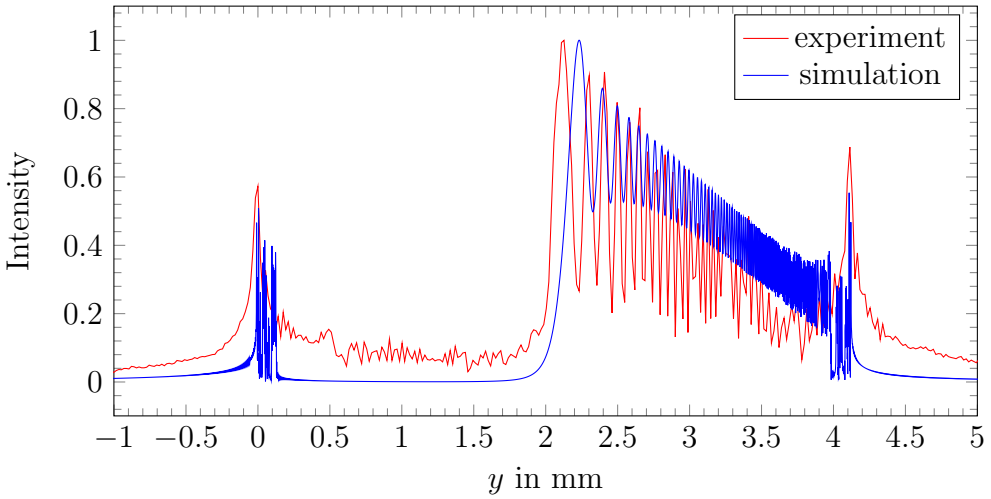

Figure 5.8.: Lineout of simulation and experiment of smaller glass capillary ($r_{o,1} = 2.065\,\text{mm}$, $r_{i,1} = 2\,\text{mm}$) in the schlieren setup taken with HNL100L.

In the lineout we can measure a diameter of $(234 \pm 2)\,\text{px}$ which corresponds to $(4.11 \pm 0.03)\,\text{mm}$. The distance is determined by the highest peak on the left and the right. This coincides with the diameter (4.13 ± 0.02) we measured at the beginning. In Figure 5.9 we zoom onto to

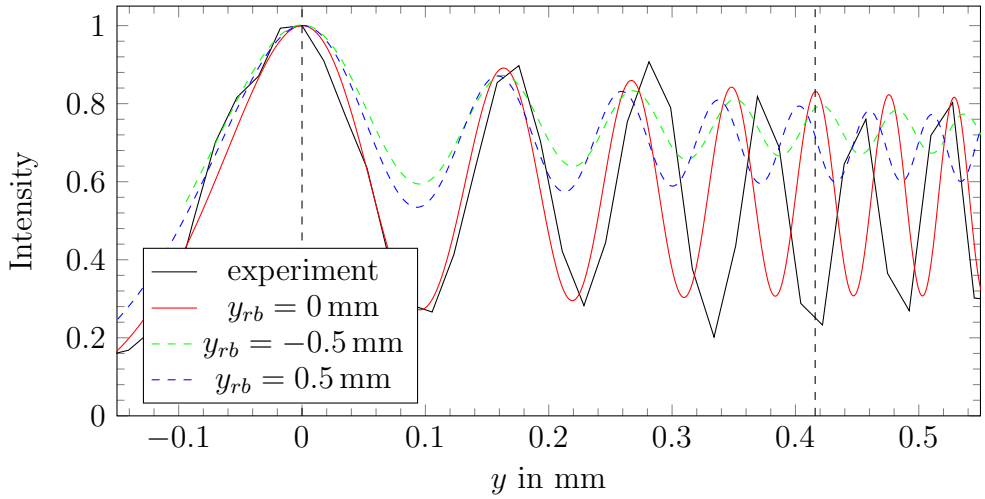

Figure 5.9.: Simulated diffraction pattern of the smaller glass capillary ($r_o = 2.065\,\text{mm}$, $r_i = 2\,\text{mm}$) in the schlieren setup. The first peak is centered around 0 mm. The dashed plots correspond to results of the height variations of the razor blade.

the oscillating diffraction pattern at the central bright side. This diffraction pattern contains information of the focal length of the glass capillary. To find out the focal length we can perform numerical simulations of different capillaries parameters r_i and r_o and search for a pattern

similar to the experimental one. For the red curve in Figure 5.9 we set the expected parameters of the smaller glass capillary. If we measure the length between the first peak and the fifth peak we get a value of $(0.457 \pm 0.002)\,\mathrm{mm}$. For the simulation we get $(0.416 \pm 0.005)\,\mathrm{mm}$. The values do not match within the error range. We identified two possible error sources. The first one is the y-position of the razor blade. Out of the simulations we know that the razor blade position affects the spacing between the peaks of the diffraction pattern. This can be seen in Figure 5.9 where we shifted the razor blade y-position with 0.5 mm above or below the focus. A misalignment in the y-position of 0.5 mm can cause a peak distance difference of approximately 0.02 mm. A second error could be the inexact manufacturing of the glass capillary. We presented at the beginning that the error in the focal length is large due to inaccuracies in the radius values. Varying the radius r_o or r_i by 0.01 mm allows us to achieve a similar diffraction pattern. In Figure 5.10a we can see the recorded schlieren image without a target. In Figure 5.10b we inserted the larger glass capillary into the beam path. The edges of the capillary are clearly visible. The several black spots are caused by dirt on the surface on the glass capillary.

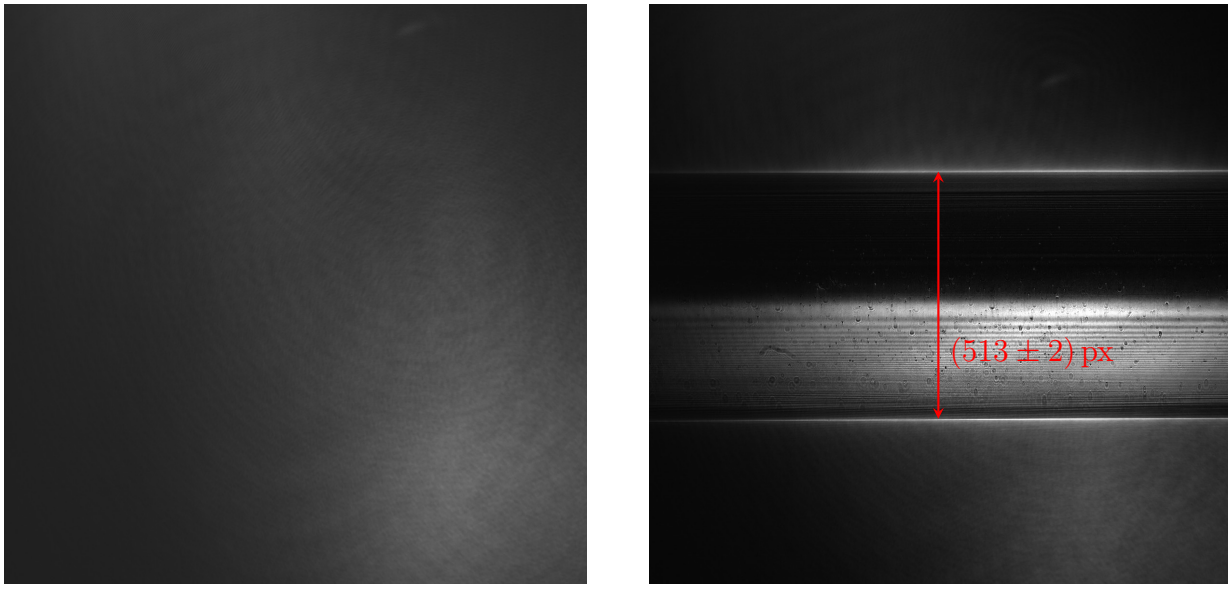

(a) With razor blade but without glass capillary (b) With razor blade and glass capillary

Figure 5.10.: Schlieren image of the larger glass capillary ($r_o = (3.00 \pm 0.02)\,\mathrm{mm}$, $r_i = (2.95 \pm 0.02)\,\mathrm{mm}$) taken with HNL100L.

In Figure 5.11 we can see a lineout of Figure 5.10. The distance between the edges is $(513 \pm 2)\,\mathrm{px}$ or $(6.01 \pm 0.02)\,\mathrm{mm}$. These values agree well with the values of the manufacturer. In Figure 5.11b we subtract the signal without glass capillary from the signal with glass capillary. The signal does not change its general structure and we can still recognize the bright edges.

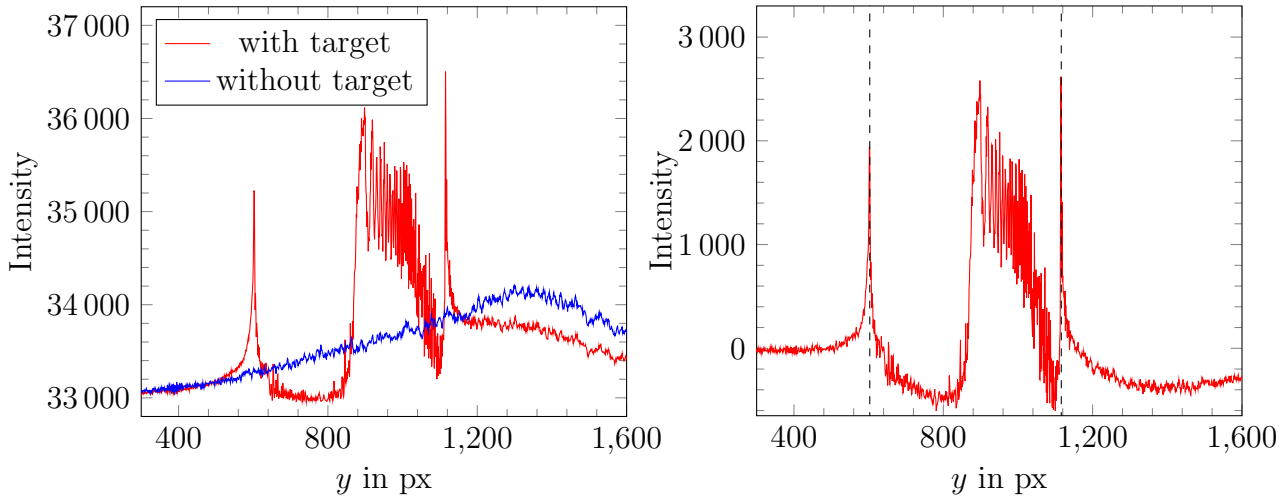

(a) Lineout of Figure 5.10a and Figure 5.10b

(b) Difference between both lineouts

Figure 5.11.: Lineouts of the schlieren images of the larger glass capillary ($r_o = (3.00 \pm 0.02)$ mm, $r_i = (2.95 \pm 0.02)$ mm).

5.3.2. Shadowgraphy Imaging

Our last experiments are the shadowgraphy measurements on the glass capillaries. The setup is shown in Figure 3.7.

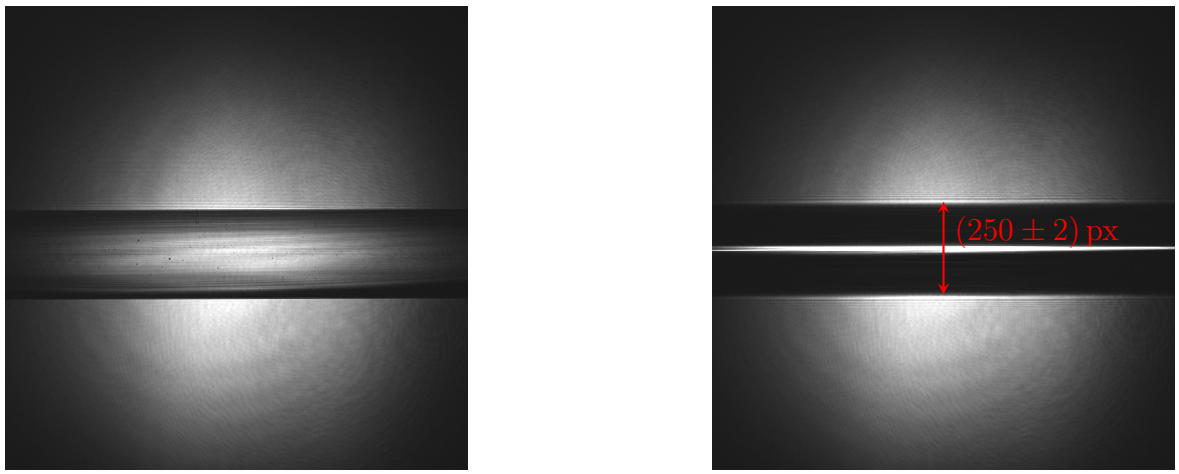

(a) Image taken at a distance of (0 ± 5) mm in front of the target

(b) Image taken at distance (65 ± 5) mm in front of the target

Figure 5.12.: Shadowgraphy image of the smaller glass capillary ($r_o = (2.065 \pm 0.020)$ mm, $r_i = (2.00 \pm 0.02)$ mm) taken with HNL100L.

A relay imaging system was used to place the camera with a distance in front of the target because the glass capillary has a negative focal length and the focused line is only virtually. The

image acquired at the focal plane of the capillary can be seen in Figure 5.12a. In Figure 5.12b the focal line is visible. We measured a value of (-65 ± 5) mm for the focal length of the capillary. This confirms the value we calculated with Equation 3.11. For the diameter we measure a value of (250 ± 2) px or (4.40 ± 0.03) mm. This is a 10% deviation from the real value. This is the same diffraction effect already mentioned in Figure 4.18. In Figure 5.13 we can see the development of the shadowgraphy images for the second glass capillary. Due to the spherical aberrations it is not very precise to determine the focal length. Inspecting the different images in Figure 5.13 we see for (170 ± 20) mm a well focused line. The diameter is (374 ± 2) px or (6.57 ± 0.04) mm. Again there is a 10% deviation due to diffraction.

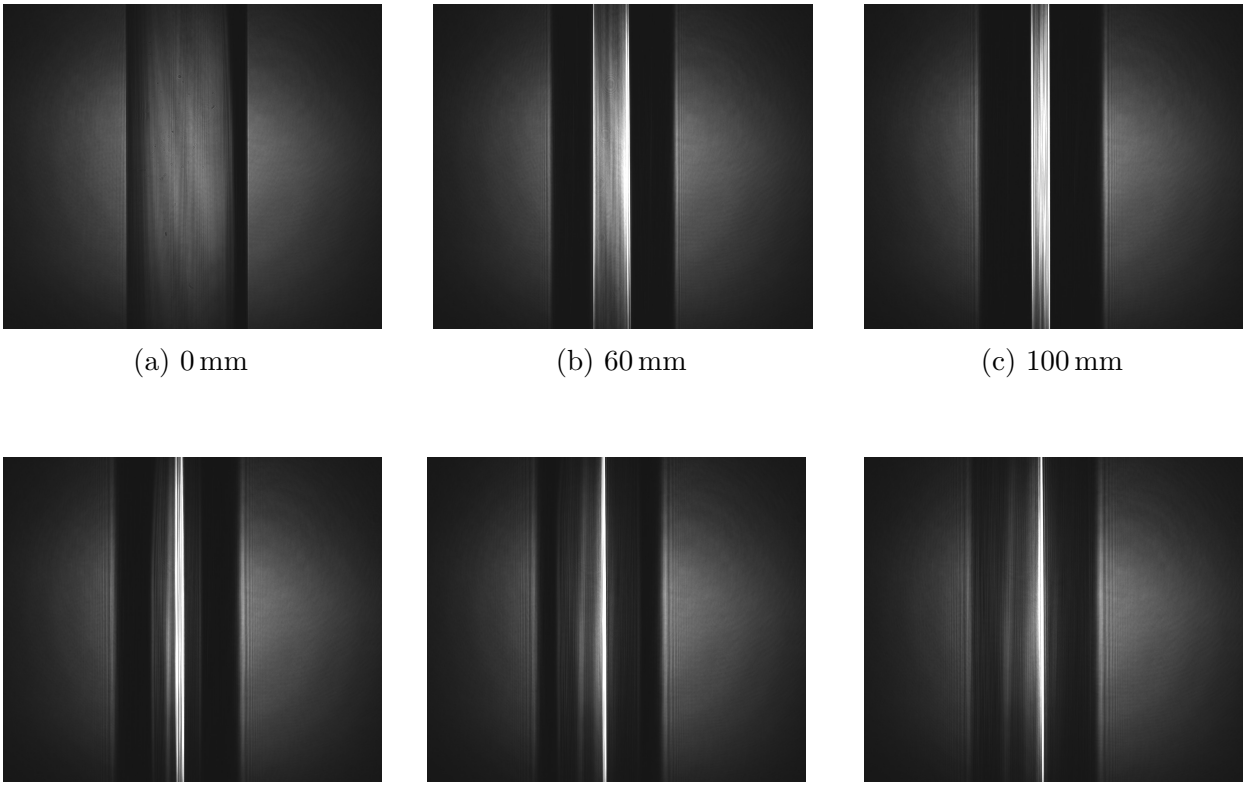

(a) 0 mm (b) 60 mm (c) 100 mm

(d) 140 mm (e) 170 mm (f) 200 mm

Figure 5.13.: Shadowgraphy image of the larger glass capillary ($r_o = (3.00 \pm 0.02)$ mm, $r_i = (2.95 \pm 0.02)$ mm) taken with HNL100L.

6. Conclusion

The advanced wakefield experiment accelerates electrons in a plasma wakefield with a proton bunch as driver through a 10 m long rubidium plasma. In this thesis we theoretically analyze the optical properties of a plasma column, a fuzzy plasma column, a cylindrical lens and a glass capillary. The latter two are used as benchmark targets in experimental measurements. Simulations and experiments with the schlieren setup confirm the possibility to determine the diameter of the targets column up to several ten micrometers. From the diffraction pattern it is also possible to estimate the focal length.
Using the shadowgraphy setup one can determine the diameter of the column. Though simulations show that a radius of ≈ 1 mm can cause diffraction effects which introduce significant deviations in the diameter determination. Focal length measurements are more precise with the shadowgraphy setup. If one measures the refractive index of the rubidium column via a separate measurement, the focal length is also directly connected to the radius of the column. Hence, the focal length measurement can also be used to determine the radius.

A. Basics of Computational Wave optics

Most parts of this chapter were already written and submitted for my Bachelor's Thesis in Computer Science at the Technical University of Munich [Wec18].

In this chapter we want to explain more details about the numerical simulation of wave optics.

A.1. Scalar Diffraction Theory

Light is an electromagnetic field which has components in all three directions. However, in most cases it is enough to solve diffraction problems with a scalar approach. In general, diffraction integrals quantify the situation when an electromagnetic wave hits an aperture and we want to know the electric field behind the aperture. All these equations can be derived out of Maxwell's

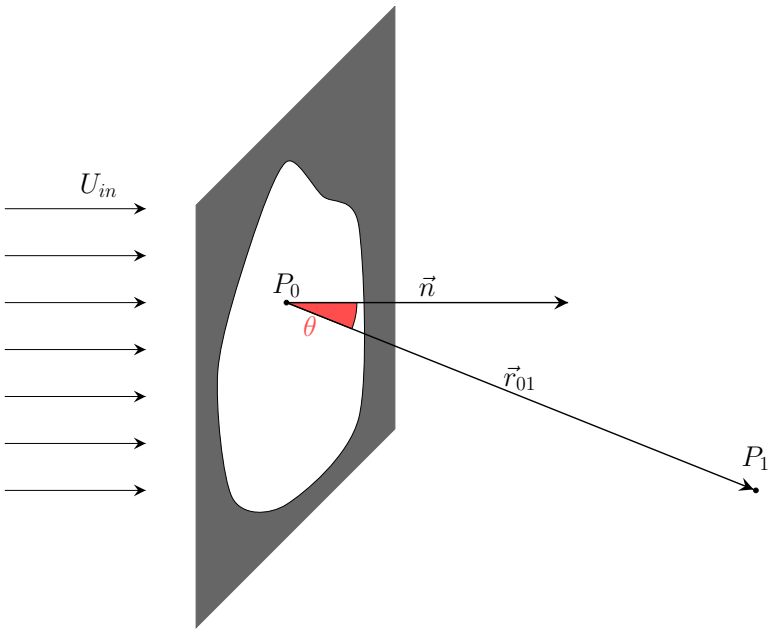

Figure A.1.: Diffraction of an aperture

equations and a full treatise can be found in [Goo96] or [Gu00].

Depending on which boundary conditions are chosen three different solutions exist which are named Rayleigh-Sommerfeld I, II and Kirchhoff integral. In [WM64] it was shown that for an aperture much larger than the wavelength and for moderate angles all theories are identical. For simplicity we choose Rayleigh-Sommerfeld I:

$$U(P_1) = \frac{1}{i\lambda} \iint_{\Sigma} U(P_0) \frac{\exp(ikr_{01})}{r_{01}} \cos(\theta)\, \mathrm{d}s \tag{A.1}$$

θ is the angle between the normal vector of the aperture and the vector $\vec{r}_{01}$. The cos-obliquity factor is sometimes set to 1. Σ is the aperture which is hit by the wave. The scenario is drawn in Figure A.1. Later we'll use the integral in rectangular coordinates:

$$U(x, y, z) = \frac{z}{i\lambda} \iint_{\Sigma} U(\xi, \eta) \frac{\exp(ikr)}{r^2}\, \mathrm{d}\xi \mathrm{d}\eta \tag{A.2}$$

where $r = \sqrt{z^2 + (\xi - x)^2 + (\eta - y)^2}$.

Fresnel Diffraction

To get an analytical expression of more complex situations we do some approximations on Equation A.2. We want to use first order Taylor series to approximate the square root. It is valid to write $\sqrt{a+b} \approx a(1 + \frac{b}{2a})$ if $b \ll a$. In our case we can use this relation by requiring $z^2 \gg x^2 + y^2$. Using this condition we also can substitute r in the denominator by z. All together this simplifies the integral to:

$$U(x, y, z) = \frac{\exp(ikz)}{i\lambda} \int_{-\infty}^{\infty} \int_{-\infty}^{\infty} P(\xi, \eta) U(\xi, \eta) \frac{\exp\left(\frac{ik}{2z}\left((x - \xi)^2 + (y - \eta)^2\right)\right)}{z}\, \mathrm{d}\xi \mathrm{d}\eta \tag{A.3}$$

The integral over the aperture Σ can be replaced by infinite integrals over a pupil function P.

A.2. Lens as Phase Transformer

In wave optics we need a different description of a lens because the standard rules do not apply anymore. As previously shown a wave has an amplitude and a phase. Here we assume an ideal, thin lens which does not reflect any intensity. The wave number depends on the medium the wave is propagating through. In air the wave number is given by $k = \frac{2\pi}{\lambda}$ and in another medium by $k_n = n \cdot k$ where n is the refraction index. For a lens made of glass n is around 1.5. Due to this different wave number there will be a optical path difference between light passing through glass and light passing through air. If we neglect reflected intensity (Fresnel

equations describe intensity change) there will be only a phase shift. This change is described by the transmission function $t_l(x, y)$ which we want to derive. Simply said a lens is nothing else than a phase transformer.
Furthermore, we assume that incoming and emerging points of the wave through the lens are identical. This assumption is valid if we use a thin lens and paraxial rays.
A wave travelling distance d in air has the phase shift $\phi = d \cdot k$. To get the phase of the wave travelling through the lens in Figure A.2b we add the different stages of travelling through air and the lens together to

$$\phi = k\,(d - b - \Delta_1 - \Delta_2) + k\,n\,(\Delta_1 + \Delta_2 + b) \tag{A.4}$$

where Δ_2 is the small part drawn in Figure A.2c, Δ_1 is the part of the left part of the lens respectively. Using Pythogoras' theorem we obtain

$$\Delta_{1/2} = R_{1/2} - l_{1/2} = R_{1/2} - \sqrt{R_{1/2}^2 - h^2} = R_{1/2} - \sqrt{R_{1/2}^2 - (x^2 + y^2)} \tag{A.5}$$

where x, y are the positions on which the wave impacts the lens. $h^2 = x^2 + y^2$ is given by the front view in Figure A.2a. Finally, the phase shift due to the lens is:

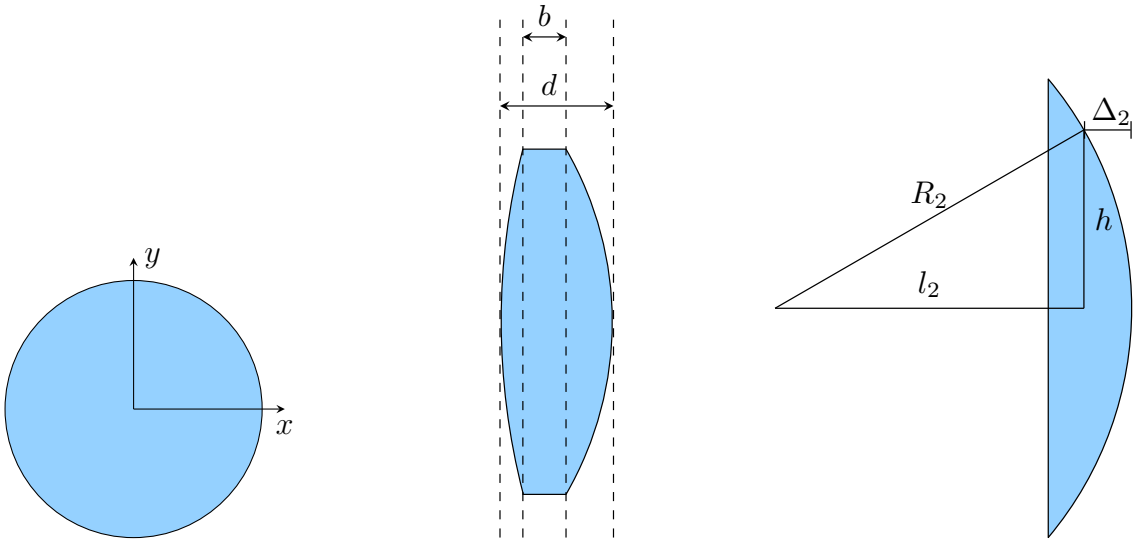

(a) front view lens (b) side view lens (c) right part of lens

Figure A.2.: Ideal thin lens

$$\begin{aligned}\phi = & k\,(n-1)\left(R_1 - \sqrt{R_1^2 + (x^2+y^2)}\right) \\ & + k\,(n-1)\left(R_2 - \sqrt{R_2^2 + (x^2+y^2)}\right) \\ & + k\,(n-1)\,b + kd\end{aligned} \tag{A.6}$$

A global phase for a wave can usually be omitted. Therefore, the last term can be removed. Again we approximately express the square root via the first order of the series $\sqrt{R_1^2 + (x^2+y^2)} \approx R_1\left(1 + \frac{x^2+y^2}{2R_1^2}\right)$. This simplifies the term to:

$$\phi = -k\,(n-1)\,\frac{x^2+y^2}{2}\left(\frac{1}{R_1} + \frac{1}{R_2}\right) \tag{A.7}$$

Now we can insert Lensmaker's equation which defines the focal length of a lens:

$$\frac{1}{f} = (n-1)\left(\frac{1}{R_1} + \frac{1}{R_2}\right) \tag{A.8}$$

This finally gives the complex transmittance

$$t_l(x,y) = \exp\left(-i\,\frac{k}{2f}\,(x^2+y^2)\right). \tag{A.9}$$

This expression was derived for a double-convex lens but according to [Goo96] it is also true for other types of lenses like double-concave.

A.3. Fourier Property of a Lens

In the previous parts we introduced the transmittance function of a lens and the Fresnel diffraction. Based on these concepts we can derive the Fourier property of a thin lens. This property is especially important to allow fast numerical calculations of optical systems.

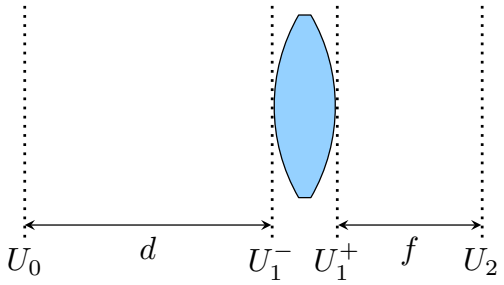

Figure A.3.: Thin lens

Figure A.3 shows the situation we want to model. Having a field U_0 at position d in front of the lens, we want to calculate the electrical field U_2 exactly one focal length f behind the lens. The first step is to propagate the field until the lens using Fresnel approximation. This is valid for rather small angles which we will assume now. We use Equation A.3:

$$U_1^-(x,y) = \frac{\exp(ikd)}{i\lambda}\int_{-\infty}^{\infty}\int_{-\infty}^{\infty} P(\xi,\eta)U_0(\xi,\eta)\frac{\exp\left(\frac{ik}{2d}((x-\xi)^2+(y-\eta)^2)\right)}{d}\mathrm{d}\xi\mathrm{d}\eta \tag{A.10}$$

The wave transmission through the lens is given by Equation A.9. If we plug in Equation A.10 into the lens transmission given by Equation A.9, we get the field after the lens. Furthermore we assume that the lens is quite large and we can leave out the pupil function $P(x,y)$.

$$U_1^+(x,y) = \exp\left(-i\frac{k}{2f}(x^2+y^2)\right)\frac{\exp(ikd)}{i\lambda} \tag{A.11}$$

$$\int_{-\infty}^{\infty}\int_{-\infty}^{\infty} P(\xi,\eta)U_0(\xi,\eta)\frac{\exp\left(\frac{ik}{2d}((x-\xi)^2+(y-\eta)^2)\right)}{d}\mathrm{d}\xi\mathrm{d}\eta \tag{A.12}$$

From U_1^- we do another Fresnel propagation with Equation A.3 until the back focal plane of the objective:

$$U_2(x,y) = \frac{\exp(ikf)}{i\lambda}\iint_{-\infty}^{\infty} U_1^+(\nu,\tau)\frac{\exp\left(\frac{ik}{2f}\left((x-\nu)^2+(y-\tau)^2\right)\right)}{f}\mathrm{d}\nu\mathrm{d}\tau \tag{A.13}$$

When plugging U_1^+ in, the quadratic term of the lens cancels out. Note that the exponential prefactor has now a positive sign:

$$\begin{aligned} U_2(x,y) = &\exp\left(i\frac{k}{2f}(x^2+y^2)\right)\frac{\exp(ik(d+f)}{i\lambda i\lambda}\iiiint_{-\infty}^{\infty} \\ &U_0(\xi,\eta)\frac{\exp\left(\frac{ik}{2d}((\nu-\xi)^2+(\tau-\eta)^2)\right)}{d}\frac{\exp\left(-\frac{ik}{f}(\nu x+\tau y)\right)}{f}\,\mathrm{d}\xi\mathrm{d}\eta\mathrm{d}\nu\mathrm{d}\tau \end{aligned} \tag{A.14}$$

Now we want to evaluate the integral over ν and τ. The relevant part of Equation A.14 is:

$$\iint_{-\infty}^{\infty}\exp\left(i\frac{k}{2d}\left((\nu-\xi)^2+(\tau-\eta)^2\right)\exp\left(-i\frac{k}{f}(\nu x+\tau y)\right)\mathrm{d}\nu\mathrm{d}\tau\right. \tag{A.15}$$

A substitution with $\nu' = \nu - \xi$ and $\tau' = \tau - \eta$ gives us:

$$\iint_{-\infty}^{\infty}\exp\left(i\frac{k}{2d}(\nu'^2+\tau'^2\right)\exp\left(-i\frac{k}{f}(\nu' x+\tau' y)\right)\exp\left(-i\frac{k}{f}(\xi x+\eta y)\right)\mathrm{d}\nu'\mathrm{d}\tau' \tag{A.16}$$

The first part is a scaled Fourier transform of a Gaussian. One can look that up that in calculus books:

$$\iint_{-\infty}^{\infty} \exp\left(\frac{ic}{2}(t_1^2+t_2^2)\right) \exp\left(-i(t_1\omega_1+t_2\omega_2)\right) \mathrm{d}t_1\mathrm{d}t_2 = \frac{2\pi i}{c} \exp\left(-\frac{i}{2c}(\omega_1^2+\omega_2^2)\right) \tag{A.17}$$

Using Equation A.17 we can reduce Equation A.16 to:

$$\frac{2\pi i d}{k} \exp\left(-\frac{ikd}{2f^2}(x^2+y^2)\right) \exp\left(-i\frac{k}{f}(\xi x+\eta y)\right) \tag{A.18}$$

Finally, we can plug Equation A.18 into Equation A.14 and use $k = \frac{2\pi}{\lambda}$:

$$\begin{aligned} U_2(x,y) = &\frac{\exp\left(i\frac{k}{2f}\left(1-\frac{d}{f}\right)(x^2+y^2)\right)\exp(ik(d+f)}{i\lambda f} \iint_{-\infty}^{\infty} \\ &U_0(\xi,\eta)\exp\left(-i\frac{k}{f}(\xi x+\eta y)\right)\,\mathrm{d}\xi\mathrm{d}\eta \end{aligned} \tag{A.19}$$

We can also leave out constant phase factors like $\frac{1}{i}$ and $\exp(ik(d+f))$.

$$U_2(x,y) = \frac{\exp\left(i\frac{k}{2f}\left(1-\frac{d}{f}\right)(x^2+y^2)\right)}{\lambda f} \iint_{-\infty}^{\infty} U_0(\xi,\eta)\exp\left(-i\frac{k}{f}(\xi x+\eta y)\right)\,\mathrm{d}\xi\mathrm{d}\eta \tag{A.20}$$

The result is in accordance with a different derivation in [Goo96] and is quite interesting because it says that the Fourier transform of the input field U_0 is the output field U_2 times a phase factor. However, if one chooses $d = f$ Equation A.20 reduces further to an exact (scaled) Fourier transform:

$$U_2(x,y) = \frac{1}{\lambda f} \iint_{-\infty}^{\infty} U_0(\xi,\eta)\exp\left(-i\frac{k}{f}(\xi x+\eta y)\right)\,\mathrm{d}\xi\mathrm{d}\eta = \frac{2\pi}{\lambda f}\,\mathcal{F}(U_0)\left(\frac{k}{f}x, \frac{k}{f}y\right) \tag{A.21}$$

Equation A.21 is often called Fourier property of a lens since the output field at the back focal plane is the Fourier transform of the input field at the front focal plane.

A.4. Fast Fourier Transform

In the previous part we encountered many Fourier integrals which we have to evaluate. They have the general form:

$$F(x,y) = \iint_{-\infty}^{\infty} f(\xi,\eta)\exp\left(-2\pi i b(x\xi+y\eta)\right)\mathrm{d}\xi\mathrm{d}\eta \tag{A.22}$$

At this point we take the parameter b into the argument side $\tilde{x} = bx$ and $\tilde{y} = by$ and get the slightly different integral

$$F(\tilde{x}, \tilde{y}) = \iint_{-\infty}^{\infty} f(\xi, \eta) \exp\left(-2\pi i(\tilde{x}\xi + \tilde{y}\eta)\right) \mathrm{d}\xi \mathrm{d}\eta. \tag{A.23}$$

To evaluate Fourier integrals efficiently the fast Fourier transform algorithm (FFT) was developed and in most programming languages a fast implementation is available. `MATLAB` uses `FFTW` [FJ05] and the 2D-FFT (for a vector f with length n) is defined as

$$F(k_x, k_y) = \sum_{a=1}^{n} \sum_{b=1}^{n} f(a, b) \exp\left(-2\pi i \frac{(a-1)(k_x-1)}{n}\right) \exp\left(-2\pi i \frac{(b-1)(k_y-1)}{n}\right). \tag{A.24}$$

To benefit from the FFT we have to discretize Equation A.23 and transform it to the required form (Equation A.24). First, we evaluate the integral with the Riemann sum using N steps

$$F(\tilde{x}, \tilde{y}) = \sum_{n=-N/2}^{N/2-1} \sum_{m=-N/2}^{N/2-1} f\left(\frac{Ln}{N}, \frac{Lm}{N}\right) \left(\frac{L}{N}\right)^2 \exp\left(-2\pi i \left(\frac{\tilde{x}Ln}{N} + \frac{\tilde{y}Lm}{N}\right)\right) \tag{A.25}$$

where we assume that $f = 0$ outside $\left[-\frac{L}{2}, \frac{L}{2}\right] \times \left[-\frac{L}{2}, \frac{L}{2}\right]$. This assumption is reasonable for most cases since we want to calculate diffraction effects which occur when light passes through specific finite slits or apertures.

Note that $\tilde{x}$ and $\tilde{y}$ are variables in the continuous frequency domain. Due to the FFT these variables are also discretized and the final resulting vector F is an array with the same size as the input array f. The input array is sampled with the distance between two points $\Delta\xi = \frac{L}{N}$ and therefore the maximum spatial frequencies are given by the Nyquist frequency

$$|f_{\max}| = \frac{1}{2\Delta\xi}. \tag{A.26}$$

Since we have got n data points we receive n frequencies by the FFT. Equally spaced this gives us

$$\left\{-\frac{1}{2\Delta\xi}, -\frac{1}{2\Delta\xi} + \frac{1}{L}, -\frac{1}{2\Delta\xi} + \frac{2}{L}, \ldots, \frac{1}{2\Delta\xi} - \frac{1}{L}\right\}. \tag{A.27}$$

$\tilde{x}$ and $\tilde{y}$ only take values out of this interval and we can express them with integers $p, q \in [-\frac{N}{2}, \frac{N}{2} - 1]$ with

$$\begin{aligned} \tilde{x} &= xb = \frac{p}{L} \\ \tilde{y} &= yb = \frac{q}{L} \end{aligned} \tag{A.28}$$

Inserting these expressions into Equation A.25 results in

$$F(p,q) = \sum_{n=-N/2}^{N/2-1} \sum_{m=-N/2}^{N/2-1} f\left(\frac{Ln}{N}, \frac{Lm}{N}\right) \left(\frac{L}{N}\right)^2 \exp\left(-2\pi i \left(\frac{pn}{N} + \frac{qm}{N}\right)\right). \tag{A.29}$$

With Equation A.28 we are able to calculate to which array index p the x position corresponds. The observation is that the input array describes an electrical field with input size L and the output array contains a field with side length $L_2 = \frac{N}{Lb}$. Later we will see that $b = \frac{1}{\lambda z}$ (z is the distance from aperture to screen) and this results in

$$L_2 = \frac{\lambda z N}{L}. \tag{A.30}$$

There is only one difference between Equation A.25 and Equation A.24 left due to the summation borders. The array indices p and q are currently defined from negative values to positive ones but the index from `MATLAB` is from 1 to N. The FFT definition requires the central position located at the first index of the array. Thus, we have to shift the arrays to the right position which is done with *fftshift* and *ifftshift* in `MATLAB`.
More details about the FFT in `MATLAB` can be found in [Voe11] and [Sch10].

A.5. Lens Propagation in `MATLAB`

In the previous parts we derived tools needed to calculate the propagation of light through a thin lens. In our work we used code which is similar to one of the examples in [Voe11] where the author calculates the Fraunhofer propagation of the electric field. As already shown the lens produces a Fraunhofer pattern (with some phase factors) on a screen despite the fact it was derived under Fresnel approximation. The Fraunhofer propagation is a simple Fourier transform. Requirement for this FFT propagation is an input sampling which is higher than the critical sampling otherwise the result is aliased and further propagation will create wrong patterns.
The function lensProp takes the electric field u1 at the front focal plane and the side length L1 of this field as arguments. The output is the electrical field u2 at the back focal plane.

Remarkable is the scaling of the output field. The side length L2 depends on lambda, L1, z and N given by Equation A.30.

```
function [u2, Lx2, Ly2]=lensProp(u1, Lx1, Ly1, lambda, z);
    [N, M] = size(u1);
    dx = Lx1/M;
    dy = Ly1/N;
    Ly2 = lambda * z / dy;
    Lx2 = lambda * z / dx;
    const = 1/(1i*lambda*z);
    u2 = const * fftshift(fft2(ifftshift(u1))) * dx * dy;
end
```

Listing A.1: Code for field propagation through a lens

This function assumes that N is odd because `MATLAB` is sensitive to the order of *ifftshift* and *fftshift* for odd and even input.

A.6. Fresnel Propagation in `MATLAB`

The content of this section is taken from [Sch10] and [Voe11]. Fresnel diffraction is given by Equation A.3 but we can express it alternatively in the following form:

$$U(x,y,z) = \frac{\exp(ikz)}{i\lambda z}\exp\left(\frac{k}{2z}(x^2+y^2)\right) \tag{A.31}$$

$$\int_{-\infty}^{\infty}\int_{-\infty}^{\infty} U(\xi,\eta)\exp\left(\frac{ik}{2z}\left(\xi^2+\eta^2\right)\right)\exp\left(-\frac{ik}{2z}\left(\xi x+\eta y\right)\right)\,\mathrm{d}\xi\mathrm{d}\eta \tag{A.32}$$

We recognize that the Fresnel diffraction can be represented as Fourier transform. Similar to above we obtain the final code.

```
function [x2 y2 u2] = fresnelProp(u1, Lx1, Ly1, x, y, lambda, z)

[N, M] = size(u1);
dx1 = Lx1/M;
dy1 = Ly1/N;
Ly2 = lambda * z / dy1;
Lx2 = lambda * z / dx1;

k = 2 * pi / lambda;
```

```
% source-plane coordinates
[x1 y1] = meshgrid(x, y);

% observation-plane coordinates
[x2 y2] = meshgrid(x * Lx2 / Lx1, y * Ly2 / Ly1);

% evaluate the Fresnel-Kirchhoff integral
u2 = 1 / (1i*lambda*z) ...
    .* exp(1i * k/(2*z) * (x2.^2 + y2.^2)) ...
    .* fftshift(fft2(fftshift(u1 .* exp(1i * k/(2*z) ...
    * (x1.^2 + y1.^2))))) * dx1 * dx2;
```

Listing A.2: Code for Fresnel Propagation

The main difference is the quadratic phase factor which is multiplied to the input electrical field and the second quadratic phase factor which is multiplied after the Fourier transform.

Bibliography

[Adl+18] E. Adli, A. Ahuja, O. Apsimon, R. Apsimon, A. Bachmann, D. Barrientos, F. Batsch, J. Bauche, V. Olsen, M. Bernardini, T. Bohl, C. Bracco, F. Braunmueller, G. Burt, B. Buttenschoen, A. Caldwell, M. Cascella, J. Chappell, E. Chevallay, M. Chung, D. Cooke, H. Damerau, L. Deacon, L. Deubner, A. Dexter, S. Doebert, J. Farmer, V. Fedosseev, R. Fiorito, R. Fonseca, F. Friebel, L. Garolfi, S. Gessner, I. Gorgisyan, A. Gorn, E. Granados, O. Grulke, E. Gschwendtner, J. Hansen, A. Helm, J. Henderson, M. Huether, M. Ibison, L. Jensen, S. Jolly, F. Keeble, S. Kim, F. Kraus, Y. Li, S. Liu, N. Lopes, K. Lotov, L. Brun, M. Martyanov, S. Mazzoni, D. Godoy, V. Minakov, J. Mitchell, J. Molendijk, J. Moody, M. Moreira, P. Muggli, E. Oez, C. Pasquino, A. Pardons, F. Asmus, K. Pepitone, A. Perera, A. Petrenko, S. Pitman, A. Pukhov, S. Rey, K. Rieger, H. Ruhl, J. Schmidt, I. Shalimova, P. Sherwood, L. Silva, L. Soby, A. Sosedkin, R. Speroni, R. Spitsyn, P. Tuev, M. Turner, F. Velotti, L. Verra, V. Verzilov, J. Vieira, C. Welsch, B. Williamson, M. Wing, B. Woolley, and G. Xia. "Acceleration of electrons in the plasma wakefield of a proton bunch". English. In: *Nature* 561.7723 (2018), pp. 363–367. ISSN: 0028-0836. DOI: 10.1038/s41586-018-0485-4.

[Bac+18a] A.-M. Bachmann, M. Martyanov, J. Moody, A. Pukhov, and P. Muggli. "Schlieren imaging for the determination of the radius of an excited rubidium column". In: *Nuclear Instruments and Methods in Physics Research Section A: Accelerators, Spectrometers, Detectors and Associated Equipment* 909 (2018). 3rd European Advanced Accelerator Concepts workshop (EAAC2017), pp. 387–390. ISSN: 0168-9002. DOI: https://doi.org/10.1016/j.nima.2017.12.062.

[Bac+18b] A.-M. Bachmann, J. Moody, M. Martyanov, V. Fedosseev, and P. Muggli. "Toward Determination of a Rubidium Plasma Column using Schlieren Imaging". In: *The proceedings of the COFIL2018*. 2018.

[Blu+07] I. Blumenfeld, C. E. Clayton, F.-J. Decker, M. J. Hogan, C. Huang, R. Ischebeck, R. Iverson, C. Joshi, T. Katsouleas, N. Kirby, W. Lu, K. A. Marsh, W. B. Mori, P. Muggli, E. Oz, R. H. Siemann, D. Walz, and M. Zhou. "Energy doubling of 42

GeV electrons in a metre-scale plasma wakefield accelerator". In: *Nature* 445 (Feb. 2007), 741 EP -.

[Cal+09] A. Caldwell, K. Lotov, A. Pukhov, and F. Simon. "Proton-driven plasma-wakefield acceleration". In: *Nature Physics* 5 (Apr. 2009). Article, 363 EP -.

[CER+19] CERN, Switzerland, E. Adli, A. Ahuja, O. Apsimon, R. Apsimon, A. Bachmann, D. Barrientos, M. Barros, J. Batkiewicz, F. Batsch, J. Bauche, V. Berglyd Olsen, M. Bernardini, B. Biskup, A. Boccardi, T. Bogey, T. Bohl, C. Bracco, F. Braunmüller, S. Burger, G. Burt, S. Bustamante, B. Buttenschön, A. Caldwell, M. Cascella, J. Chappell, E. Chevallay, M. Chung, D. Cooke, H. Damerau, L. Deacon, L. Deubner, A. Dexter, S. Doebert, J. Farmer, V. Fedosseev, G. Fior, R. Fiorito, R. Fonseca, F. Friebel, L. Garolfi, S. Gessner, I. Gorgisyan, A. Gorn, E. Granados, O. Grulke, E. Gschwendtner, A. Guerrero, K. Lotov, A. Sosedkin, and R. Spitsyn. "Experimental Observation of Proton Bunch Modulation in a Plasma at Varying Plasma Densities". English. In: *Physical Review E - Statistical Physics, Plasmas, Fluids, and Related Interdisciplinary Topics* 122.5 (Feb. 2019). ISSN: 0031-9007. DOI: 10.1103/PhysRevLett.122.054802.

[Dem07] W. Demtröder. *Laserspektroskopie*. Springer, 2007.

[FJ05] M. Frigo and S. Johnson. "The Design and Implementation of FFTW3". In: *Proceedings of the IEEE* 93.2 (2005). Special issue on "Program Generation, Optimization, and Platform Adaptation", pp. 216–231.

[Goo96] J. Goodman. *Introduction to Fourier Optics*. McGraw-Hill Series in Electrical and Computer Engineering: Communications and Signal Processing. McGraw-Hill, 1996. ISBN: 9780070242548.

[Gu00] M. Gu. *Advanced Optical Imaging Theory*. Springer Series in Optical Sciences. Springer, 2000. ISBN: 9783540662624.

[KPL10] N. Kumar, A. Pukhov, and K. Lotov. "Self-Modulation Instability of a Long Proton Bunch in Plasmas". In: *Phys. Rev. Lett.* 104 (25 June 2010), p. 255003. DOI: 10.1103/PhysRevLett.104.255003.

[Pie10] A. Piel. *Plasma Physics: An Introduction to Laboratory, Space, and Fusion Plasmas*. Springer, 2010.

[Sch10] J. Schmidt. *Numerical simulation of optical wave propagation: With examples in MATLAB*. Jan. 2010, pp. 1–197. DOI: 10.1117/3.866274.

[Set01] G. Settles. *Schlieren and Shadowgraph Techniques: Visualizing Phenomena in Transparent Media*. Engineering online library. Springer Berlin Heidelberg, 2001. ISBN: 9783540661559.

[Ste] D. A. Steck. *Rubidium 87 D Line Data,* `http://steck.us/alkalidata` (revision 2.1.5, 13 January 2015).

[TD79] T. Tajima and J. M. Dawson. "Laser electron accelerator". In: *Physical Review Letters* 43 (July 1979), p. 267. DOI: `10.1103/PhysRevLett.43.267`.

[Voe11] D. G. Voelz. *Computational fourier optics: A MATLAB tutorial*. Bellingham, Wash: SPIE Press, 2011.

[Wec18] F. Wechsler. "Wavefront Coding Techniques for Extended Depth of Field in Light Field Microscopy". `https://felix.sumpi.org/bachelor_thesis_felix_wechsler_cs.pdf`. Technical University of Munich, 2018.

[WM64] E. Wolf and E. W. Marchand. "Comparison of the Kirchhoff and the Rayleigh–Sommerfeld Theories of Diffraction at an Aperture". In: *J. Opt. Soc. Am.* 54.5 (May 1964), pp. 587–594. DOI: `10.1364/JOSA.54.000587`.